Czech Technical University in Prague
Faculty of Nuclear Sciences and Physical Engineering

Diploma Thesis

Study of three-particle pseudorapidity correlations of charged hadrons in Au+Au collisions in the STAR experiment

Prague, 2008 **Author: Bc. Václav Zycháček**

Supervisor: RNDr. Jana Bielčíková, Ph.D.

i Preface

Heavy-ion physics is one of the most dynamic branches of nuclear physics. Its ultimate goal is to produce and explore the new state of matter, referred to as the Quark Gluon Plasma (QGP). In the last two decades, properties of the hot and dense nuclear matter created in high energy heavy-ion collisions were substantially studied. Many new discoveries have been made and new questions have emerged.

The experiments at RHIC in BNL have been investigating this hot and dense matter which is opaque to jets, has properties of perfect liquid and carry the signature of proposed Quark Gluon Plasma.

Since the full jet reconstruction in heavy-ion environment is difficult due to the large underlying background of produced particles, leading particle correlations are commonly used.

Recently, an unexpected correlations extended in pseudorapidity, the so called **the ridge**, were observed. The origin of these pseudorapidity correlations remains an open question and is under intense theoretical and experimental investigation.

Some of the theoretical approaches connect the origin of the ridge with the longitudinal flow, which pulls the created particles together in the same direction and, as a result, it forms a long-range pseudorapidity correlation. In order to test this physics picture, the three-particle pseudorapidity correlations are a suitable method. This work focuses on this idea of collective motion in pseudorapidity direction in the STAR experiment, RHIC BNL. As a result, the verification or exclusion of longitudinal flow picture is expected.

ii Abstract

Title:
Study of three-particle pseudorapidity correlations of charged hadrons in Au+Au collisions in the STAR experiment.

Author: Bc. Václav Zycháček

Specialization: Nuclear Engineering

Sort of project: Diploma Thesis

Supervisor: RNDr. Jana Bielčíková, PhD., Nuclear Physics Institute of the ASCR.

Abstract: This work covers study of the hot and dense nuclear matter produced in Au+Au collisions ($\sqrt{s_{NN}}$ = 200 GeV) at RHIC in BNL, USA, using three-particle pseudorapidity correlation of charged hadrons with high transverse momentum. Former study of the two-particle correlations exposed unexpected long-rage correlation in pseudorapidity (”the ridge”). Nowadays, there are many theoretical models trying to explain this phenomenon. The thesis focuses on reconstruction of charged particles in TPC and subsequent analysis covering correlations, event mixing and corrections for finite detection efficiency. In the end, final results are confronted with theoretical predictions.

Key words: STAR, pseudorapidity correlations, QGP, ridge.

Název práce:
Studium tříčásticových pseudorapiditních korelací nabitých hadronů v Au+Au srážkách v experimentu STAR.

Autor: Bc. Václav Zycháček

Abstrakt: Tématem diplomové práce je studium horké a husté jaderné hmoty produkované v Au+Au srážkách ($\sqrt{s_{NN}}$ = 200 GeV) na urychlovači RHIC v BNL, USA, pomocí tříčásticových pseudorapiditních korelací nabitých hadronů s vysokým příčným impulsem. Předcházející studium dvoučásticových korelací ukázalo, že kromě očekávaných příspěvků z (mini)jetů, existují i dvoučásticové korelace s dlouhým dosahem v pseudorapiditě (”ridge”). V současné době existuje několik teoretických modelů, které se tento jev snaží vysvětlit. Práce se zabývá rekonstrukcí nabitých částic v TPC a následnou analýzou zahrnující korelace, mixování eventů a efektivitu detekce. Nakonec jsou získané výsledky diskutovány v rámci existujících teoretických modelů.

Klíčová slova: STAR, pseudorapiditní korelace, QGP, ridge.

I declare this diploma thesis was made by myself, and all used sources are mentioned in the Bibliography section.

I agree with using this piece according the law §60 n.121/2000 Czech Law Digest related the copyright issues.

In Prague, 9^{th} May, 2008.

....
signature

Contents

1 Physics of QGP

1.1 Introduction

Since the first proposal of the Relativistic HeavyIon Collider (RHIC), scientists intended to find and identify the Quark Gluon Plasma (QGP). QGP introduces the subjected matter as an early matter composed of two types of elementary particles - quarks and gluons. These were made during the first moments of the Big Bang. During the evolution of the Universe, QGP made a transition to hadronic matter governed by the law of strong interaction, Quantum Chromodynamics. QCD suggests that ordinary matter made of protons and neutrons undergoes a phase transition - to a hot plasma of quarks and gluons for temperatures larger than 10^{12}K and to a cold plasma of quarks for densities larger than 10^{12}kg.cm^{-3}. It has now become possible to carry out laboratory experiments to produce hot and dense fireballs in high-energy nucleus-nucleus collisions using heavy-ion accelerators. The dissolving of individual nucleons into QGP is expected.

Recently, an unexpected correlation extended in pseudorapidity, the so called ridge, was observed. Some of the theoretical approaches connect the origin of the ridge with the longitudinal flow, which pulls the created particles together in the same direction and, as a result, it forms a long-range pseudorapidity correlation. Quark Gluon Plasma, the new proposed state of matter, was not yet confirmed but all the analyses are in agreement with it as well as with ”regular” dense matter formed in overlap region during heavy-ion collisions. Thus, we will often refer only to QGP, but the meaning may be more general.

This work focuses on one important part in the QGP study, the three-particle correlations, used for collective behaviour investigation.

First of all, the collision between nuclei will be discussed - difference between heavy ions and small nuclei like protons. Then, the evolution of fireball is needed to be explained in short manner to cover the theoretical basics. Finally, the hard probes, jets, and their correlations will be used for the QGP investigation and the unexpected phenomena, such as an appearance of the ”ridge” will be discussed. Considerable emphasis is made to introduce several theoretical approaches in the ridge origin explanation. Consequently, for understanding of the problem, the results will be confronted with the newest theoretical findings and predictions.

1.2 Heavy Ion Collision

1.2.1 Evolution of Heavy Ion Collision

In following paragraph, the time evolution of central AA collision will be discussed. It is schematically drawn in the Figure 1 and 2.

The possibility of the dense hot nuclear matter creation in heavy-ion collisions is proposed, and experimentally confirmed. It is a result of collision of heavy Lorentz-contracted relativistic nuclei. Incoming nucleons lose their kinetic energies in these collisions, converting the energy into other degrees of freedom. The amount of energy lost during the collisions depends on the thickness of the nuclei and also on the collision energy. The degree of energy loss is called the nuclear **stopping power**. At relativistic energies, the stopping power shows a saturation effect - the incident particles do not lose all their kinetic energy, but punch through the opponent nucleus.

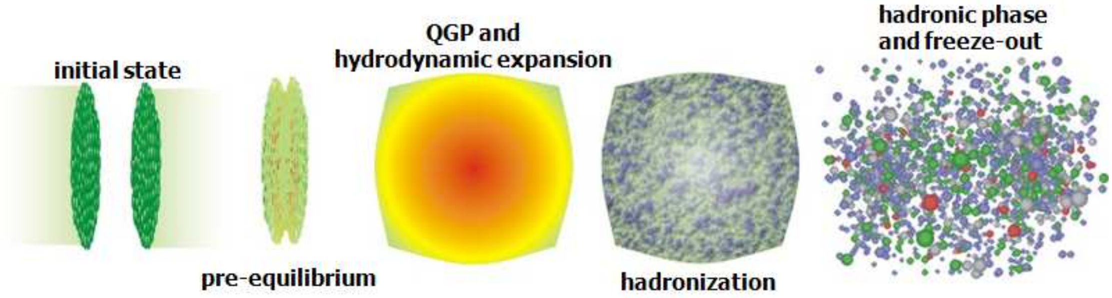

Figure 1: Schematic evolution of relativistic nucleon-nucleon collision and its evolution.

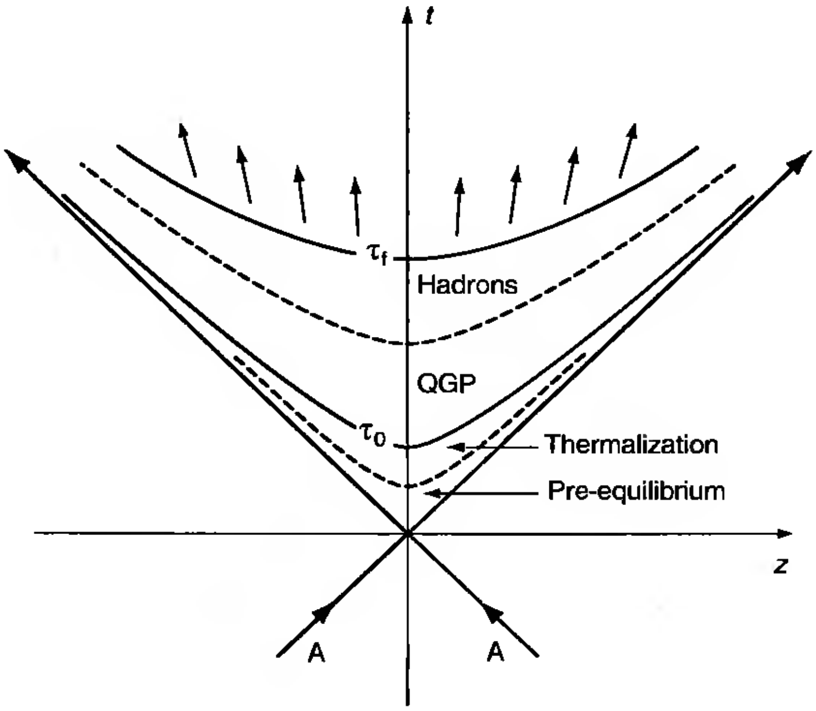

Figure 2: Light cone diagram showing the longitudinal evolution of an ultra-relativistic nucleus-nucleus collision. Constant hyperbolas contours represent a constant proper time τ [4].

After a head-on collision of two beams of nuclei, many virtual quanta and gluon fields are excited. Simultaneously, a certain amount of entropy is produced. However, its exact amount and subsequent thermalization is still unknown. Thus, it is predicted that the entropy strictly depends on the degrees of freedom.

It takes a certain de-excitation time τ_{de} to form real quarks and gluons. The de-excitation time is typically assumed to be in fraction of 1 fm. The state of matter for $0 < \tau < \tau_{de}$ is called the **pre-equilibrium stage.**

The real partons produced during the de-excitation process interact with each other and constitute an **equilibrated plasma (QGP).** In time $\tau_{de} < \tau_0 < \tau_f$, the system is thermally equilibrated and the relativistic hydrodynamics notion can be used to describe this state of matter. Using lattice QCD, time evolution until freezout time $\tau = \tau_f$ can be predicted. τ_0 depends not only on the basic parton-parton cross section, but also on the density of partons produced in the pre-equilibrium stage. The order of τ_0 is assumed to be of 1 fm.

The highly excited matter produced consequently cools down and then **hadronizes** into mesons and baryons, which are eventually observed in the detectors. This is done via freeze-out of the hadronic plasma at a τ_f time. It is defined by a space-time hyper-surface (see Figure 2), where the mean free time of the plasma particles becomes larger than the time scale of the plasma expansion so the local thermal equilibrium is no longer maintained. There are two kinds of freeze-outs. **The chemical freeze-out,** when the number of each species is frozen while the equilibration in the phase-space is maintained. **The kinetic freeze-out,** after which the kinetic equilibrium is no longer maintained. The chemical freeze-out temperature must be higher than that of the kinetic one. Also, these temperatures depend on the hadronic species in principle.

1.2.2 Collision Geometry, Centrality

The center of mass of the two colliding nuclei sets the origin in momentum space, the collision point sets the origin along the beam direction in coordinate space. Initially, the nuclei travel parallel to the z-axis with opposite momenta. The plane orthogonal to the z-axis, noted by the x and y is called **the transverse plane**. If the collision is not central but the centers of the nuclei are displaced by a finite **impact parameter b**, x axis is set to point towards the impact parameter direction. The z-axis and b direction then define **the reaction plane** (Figure 6).

Energy deposition in the reaction region is most efficient in central collisions, and by going to finite impact parameters, less entropy/energy is produced in the collision. Furthermore, changing the centrality changes the size of the system. This in turn is suitable for probing medium effects. Colored particles which travel through a background field of a strongly interacting medium experience characteristic energy loss, which rises with the volume of the medium being passed.

Nucleons with mass number **A**, which interact at least once in the collision are called **participants.** Their number is supposed to be responsible for the bulk of soft particle production and energy deposition in nuclear collisions. To express the density of participants in the transverse plane we use [35]

$$n_{part} = 2T_A(r)\left(1 - \left(1 - \frac{\sigma_0 T_A(r)}{A}\right)^A\right)$$

where $r = \sqrt{x^2 + y^2}$ is the radial distance from the origin, nucleon cross section σ_0 and T_A is the **Glauber thickness function**

$$T_A(x, y) = \int dz \rho_A(x, y, z). \tag{1}$$

The $\rho_A(x, y, z)$ term is a Wood-Saxon parametrization of the density distribution of the two nuclei with mass number A. Integrating the density of participants over the transverse plane yields, **the total number of participants** as function of the impact parameter

$$N_{part}(b) = \int dx\ dy\ n_{part}(x, y; b).$$

In heavy nuclei collisions, when partons suffer their first collision, they travel through the nuclear medium and are eligible for further (hard) collisions with other partons. This leads to the notion that one has to count the **binary collisions**, and the density of their occurrence in the transverse plane is expressed by the product of the Glauber thickness function (Eq.(1)) of one nucleus with the encountered opacity of the other nucleus, leading to the squared thickness function

$$n_{bin}(r) = \sigma T_A^2(r)$$

in symmetric and central collisions. The total number of binary collisions

$$N_{bin}(b) = \int dx\ dy\ n_{bin}(x, y; b) \tag{2}$$

also shows significant sensitivity on the impact parameter.

1.2.3 p+p vs. Au+Au Collisions, Jet Quenching

In heavy-ion collisions (e.g. at RHIC), a significant number of particles with large transverse momentum (p_T) originate from the hard scattering of quarks and gluons during the initial stages of the collision. Hard scattering is characterized by a large momentum transfer, leading to a high momentum parton (quark or gluon) traveling transverse to the beam. Hard-scattered partons fragment into a narrow cone of hadrons, referred as jet.

A large momentum transfer results from a close interaction between quarks or gluons. Since the strength of the interaction decreases with shorter distances, the cross-section for such processes can be reliably calculated by a pertubative QCD. What is important, hard-scattered partons are extremely sensitive to the medium through which they travel. In a dense quark deconfined medium, the partons are expected to have significant energy loss as they escape the system. The process of energy loss is also known as **jet-quenching**. In principle, it is sensitive to the density profile of the surrounding matter, its state of confinement and its overall size.

The most direct way to search for evidence of jet-quenching is to compare the production rate of high transverse momentum hadrons in heavy-ion collisions (Figure 4) with those in proton-proton collisions (Figure 3). In p+p collisions, there is no surrounding matter to influence the production of jets. To measure the suppression or enhancement of particles during their passing through nuclear matter, very simple method is used.

First, the number of binary collisions (Eq.(2)) occurring in a Au+Au event is calculated in a classical superposition way using Glabuer model [35]. This provides a number by which the proton-proton data can be scaled to obtain the expected transverse momentum distribution of hadrons in the absence of jet-quenching or any nuclear effects. Then, the transverse momentum distribution of hadrons in heavy-ion collisions is divided by this scaled p+p distribution. This proportion is called **Nuclear modification factor** (R_{AA}), schematically written as (3).

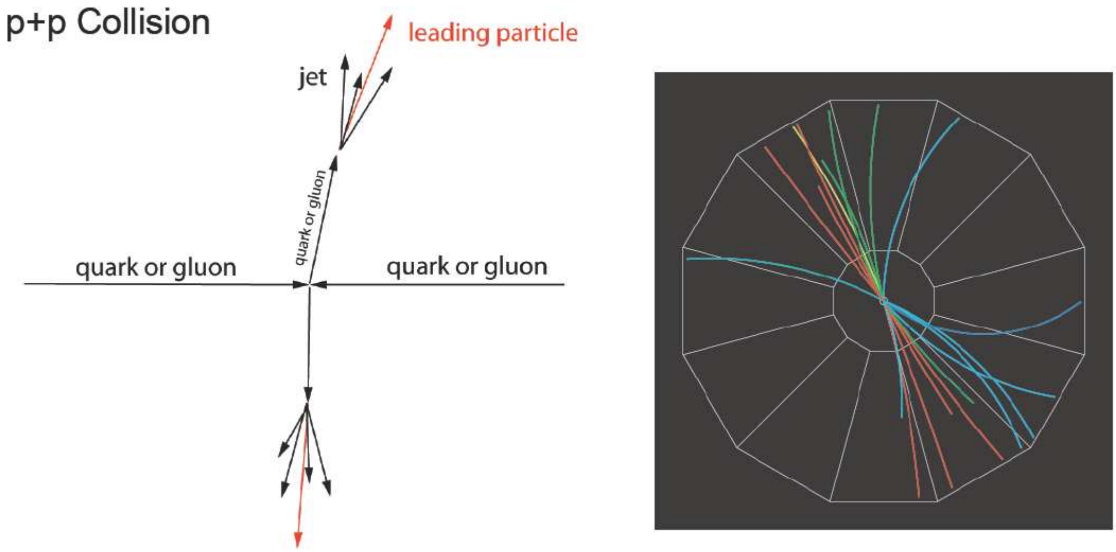

Figure 3: **Left:** schematic p+p collision, all partons (and particles) exit interaction immediately after impact, tracks can be reconstructed entirely to the interaction point. No dense matter is formed. **Right:** p+p event recorded by the STAR TPC.

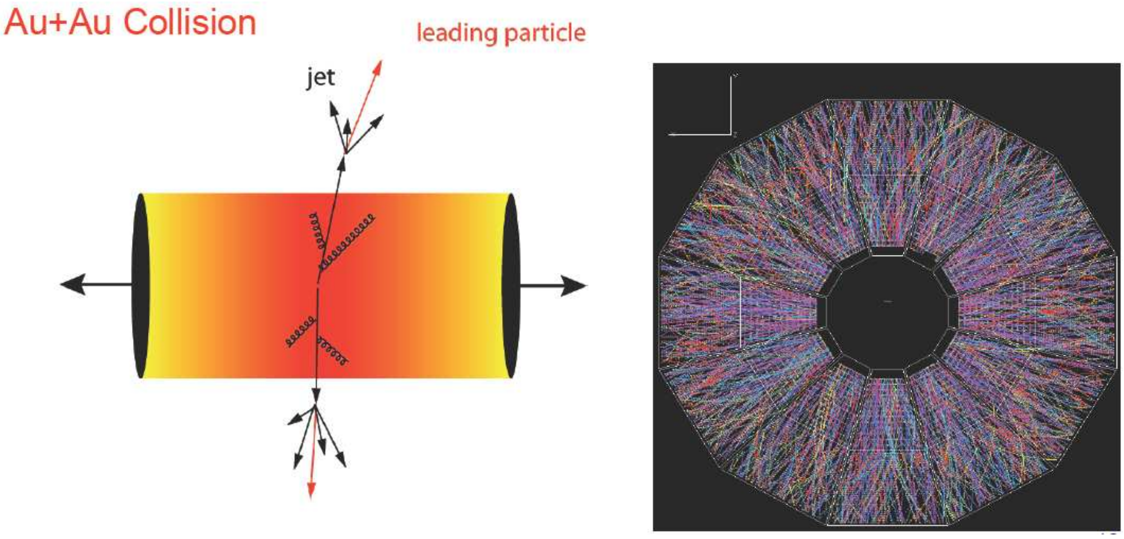

Figure 4: **Left:** schematic ion+ion collision, all partons (and particles) must more or less transverse through nuclear matter. The escaping particles and jets carry the information about the passed matter via interacting with it. **Right:** Au+Au event recorded by the STAR TPC.

$$R_{AA} = \frac{d^2N_{AA}/dp_Tdy}{< N_{coll} > \times\ d^2N_{pp}/dp_Tdy} \tag{3}$$

A value of the ratio greater than unity would correspond to an enhancement with respect

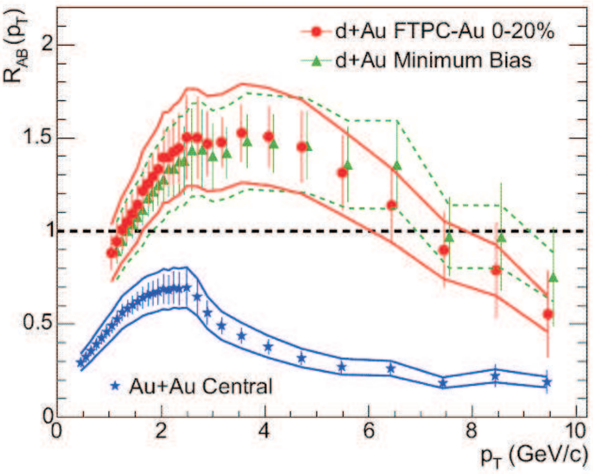

Figure 5: Nuclear modification factor for d+Au and Au+Au collisions at $\sqrt{s_{NN}} = 200$ GeV scaled by the spectrum in p+p. [30]

to a superposition of independent nucleon-nucleon collisions, whereas a value less than unity would correspond to a suppression of particle production. Experimental result is plotted in Figure 5 with evident Au+Au suppression in comparison with d+Au data, particulary for the higher p_T. This suppression is a measurable jet-quenching property, which is caused by the particle interaction with matter when passing through it [37].

1.2.4 Elliptic Flow

So far, we were not concerned by the geometric aspect of the collision. Only central collisions were assumed. Effects for the impact parameter $b \neq 0$ must be also considered.

In a non-central collision, a dense hot matter is formed in the almond-shaped region. Particles are produced and emitted from this region (Figure 6). As in the above mentioned QGP system, the overlap region can be treated by hydrodynamical description. In its view, the pressure gradient ∇P generates a collective flow (by applying the conservation of the energy and momentum: $\partial_\mu T^{\mu\nu} = 0$). In the almond shaped region, the pressure gradient is expected to be steeper in the direction of the impact parameter b (Figure 6), and the collective motion will be developed in this direction. Thus, the particle production will have an elliptical azimuthal (ϕ) distribution. Since the elliptic flow is significant at RHIC energies, it must be measured in order to detect the existence of the QGP pressure and phenomena in the early stage. The collective motion can be also used to determine whereas the phase transition is of first or higher order.

Moreover, the elliptic flow alone is a suitable probe for possible measurement of the partonic degrees of freedom as a result of quark deconfinement in QGP (see Figure 7 and 8). These observations shows independent scaling of mesons and baryons. That means that the constituents of which baryons and mesons are made of also flow independently in the medium.

Experimentally, the azimuthal distribution of particle emission is analyzed with respect to the reaction plane (Figure 6) in terms of a **Fourier expansion** as follows:

$$E\frac{d^3N}{d^3p} = \frac{d^2N}{2\pi p_T dp_T dy}\left(1 + \sum_{n=1}^{\infty} 2v_n cos[n(\phi - \Phi_r)]\right) [36] \quad (4)$$

where ϕ is the azimuthal angle of the particle and Φ_r is the azimuthal angle of the reaction plane in the laboratory frame. The first two coefficients in the Fourier decomposition are called the **directed** and **elliptic flow**. Therefore, the v_1 quantifies the strength of the directed flow ($v_1 = \langle cos\phi \rangle$), whereas v_2 quantifies the strength of the elliptic flow ($v_2 = \langle cos2\phi \rangle$). The correct reaction plane determination is a key factor in the flow measurement by method established by Eq.(4).

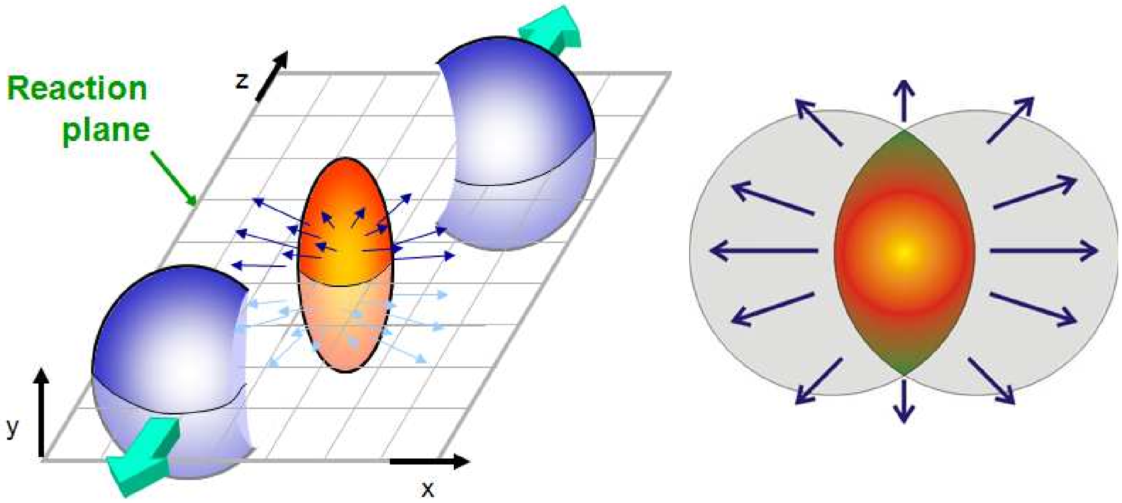

Figure 6: Schematics of non-central nuclear collision. Gradients of almond shaped surface will lead to preferential emission in the reaction plane. Defined reaction plane is indicated. Momentum vector diagram in the dense overlap region as predicted by hydrodynamics.

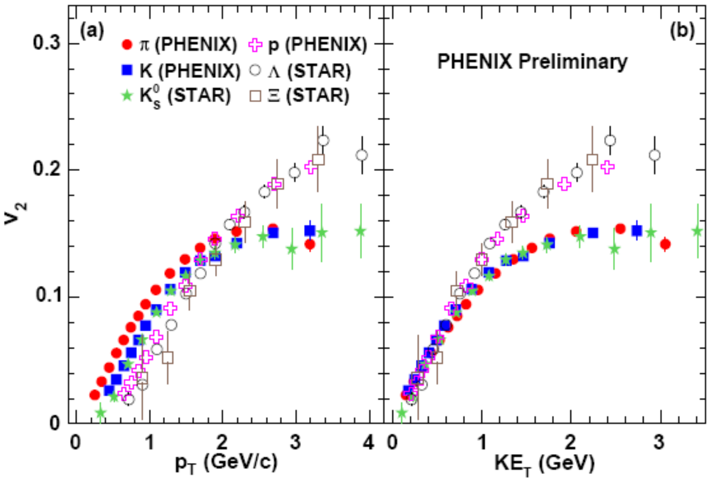

Figure 7: Variation of v_2 with (a)p_T and (b)$KE_T = m_T - m$ for several identified particles from STAR and PHENIX experiments. In the left panel, mass ordering of $v_2(p_T)$ can be observed up to $p_T \sim 2$ GeV/c - the heavier particle, the smaller its v_2. In the right panel the scaling breaks for larger values of KE_T. But the striking trend is that the mesons and baryons scale independently for the whole KE_T range. This pattern suggests that the constituents of which baryons and mesons are made also flow [19].

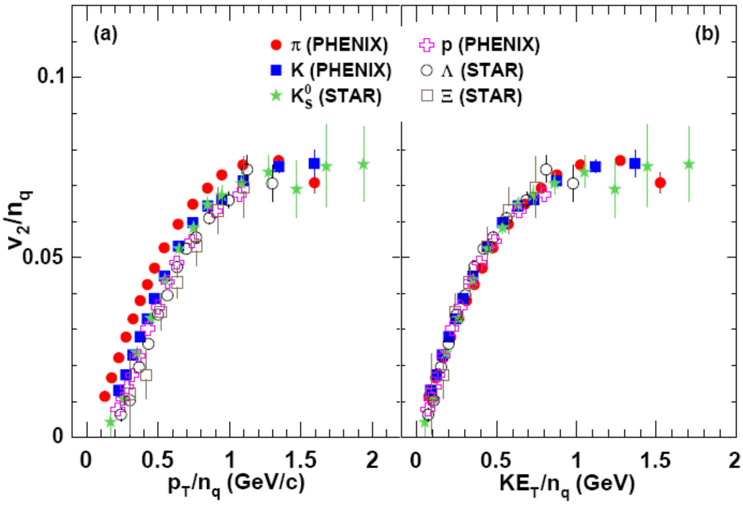

Figure 8: Values of v_2, p_T and KE_T (like in Figure 7) for different particle species are divided by their respective number of quarks. This observation can be interpreted as a strong indication that the pertinent degrees of freedom in the flowing high energy density matter are linked to the number of constituent quarks of the hadrons [19].

1.3 Two-Particle Azimuthal Correlations

Since this thesis is focused on three-particle correlations, it is appropriate to introduce the two-particle correlations first. The introduction to jet definition and jet "reconstruction" will be presented. Then, azimuthal 2-particle correlation will be showed and consequently the expansion into pseudorapidity space will be made.

In the beginning, a **jet** in heavy nuclear physics must be defined. In elementary proton-proton collisions, no dense matter is formed, and created/reflected partons emerge from the impact point, hadronising into particles forming a cone-shaped cluster along the way from the interaction point. However, in heavy-nuclear collisions, the full jet reconstruction is difficult due to the underlying background of produced particles. Therefore, a different method is applied to study jet-like processes.

First, a high p_T **leading particle** which is referred to as **the trigger particle** is identified. It is supposed to carry a major fraction of jet energy and also maintains the most probable direction of the the jet. Then, the azimuthal distribution of other particles with respect to the trigger particle, called **associated particles**, is studied. The azimuthal distribution ($\Delta\phi$) near the leading particle shapes jet-like peak, also called **a near-side peak**. At the opposite side ($\Delta\phi \approx \pi$ angle corresponds to back-to-back scattering) is jet-like peak called **an away-side peak**.

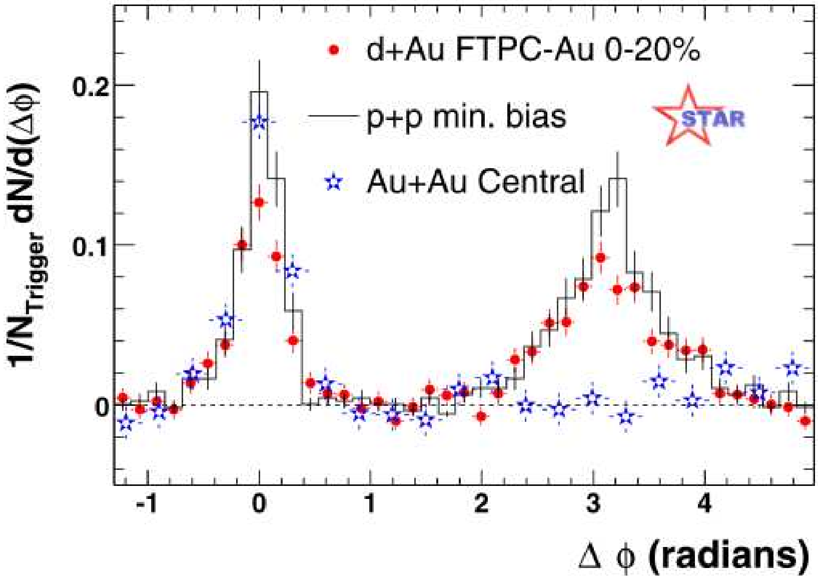

Figure 9: Comparison of two-particle azimuthal distributions for central d+Au collisions to those seen in p+p and central Au+Au collisions at $\sqrt{s_{NN}} = 200$ GeV. The respective pedestals and elliptic flow was subtracted. The disappearance of the away side peak in Au+Au collision is evident [21].

Such experimentally measured azimuthal distributions are shown for p+p, d+Au and Au+Au collisions at $\sqrt{s_{NN}} = 200$ GeV in Figure 9.

The small-angle correlations observed in p+p and d+Au collisions and at all centralities of Au+Au collisions are characteristic for hard-scattering processes already observed in elementary collisions. A strong back-to-back correlation exists for p+p and d+Au and peripheral Au+Au (not shown in Figure 9). In contrast, the back-to-back correlations are reduced considerably in the most central Au+Au collisions, indicating substantial interaction as the hard-scattered partons or their fragmentation products traverse medium.

High energy partons propagating through matter are predicted to lose energy via induced gluon radiation, with the total energy loss strongly dependent on the color charge density of the medium. This process can provide a sensitive probe of the hot and dense matter generated early in the ultrarelativistic nuclear collision (QGP phase). The hard scattering and subsequent fragmentation of partons generates jets of correlated hadrons.

To sum up, azimuthal two-particle correlations can be used for further study of the hot dense nuclear matter in heavy-ion collisions. The observed suppression of hadrons occurred as an away-side peak disappearance can be a hint in study of effects inside this matter.

1.4 Ridge Phenomenon

In addition to the two-particle correlation measurement of charged hadrons in azimuthal angle, new phenomenon in Au+Au collisions was revealed - the presence of an additional long-range pseudo-rapidity correlation on the near-side, commonly referred to as **the ridge**. It can be displayed by expanding azimuthal correlations also into pseudo-rapidity (see Figure 10). Such extended new pseudo-rapidity correlations are absent in p+p and d+Au collisions (see Figure 11). It is expected that further studies of two-particle correlations and recently introduced three-particle correlations will help to understand processes relevant to the ridge origin.

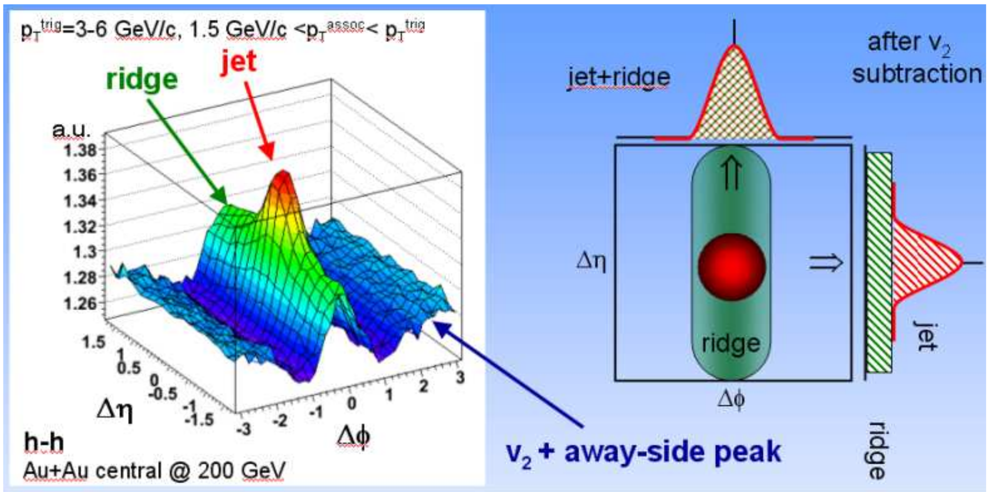

Figure 10: **Left:**Azimuthal and pseudo-rapidity correlation in Au+Au $\sqrt{s_{NN}}$ = 200 GeV collision. Long-range $\Delta\eta$ correlation at near-side, the ridge, is highlighted. **Right:** Sketch of the near side yield decomposition into jet and ridge components.

1.4.1 Origin of the Ridge

The ridge phenomenon study is a challenging question both, theoretically and experimentally. As far as it is known in nuclear collisions, there are jet-like correlations at small angular separation ($\Delta\eta \sim 0, \Delta\phi \sim 0$ in Figure 10) as well as correlations back-to-back in azimuth ($\Delta\phi \sim \pi$) but broad in $\Delta\eta$ which are presumed to result from recoil jets and elliptic flow. The new aspect is the additional correlation in central Au+Au which is short-range in azimuth ($\Delta\phi \sim 0$) but long-range in pseudorapidity ($\Delta\eta$). Several theoretical approaches are

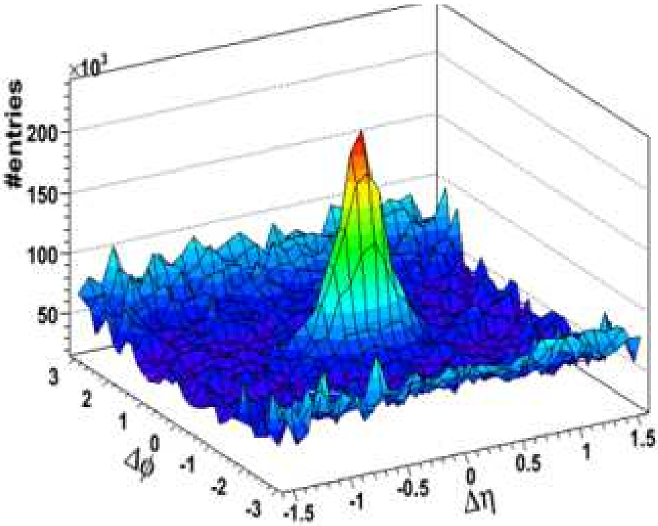

Figure 11: Azimuthal and pseudo-rapidity correlation in p+p collision. No ridge in near-side is present. [34]

attempting to explain this effect. Below, the short description of some of them relevant to this thesis is given.

- **Parton Radiation and its Coupling to the Longitudinal Flow** [26]

  This model assumes dense medium, which possesses strong collective flow component formed in heavy nucleus-nucleus collisions.

  At collider energies, the production of high-p_T hadrons and jets provides a novel independent characterization of the medium produced in nucleus-nucleus collisions. This is so since the gluon radiation off parent partons is sensitive to the interaction between the partonic projectile and the medium. The model suggests that parton energy loss is sensitive to both the energy density ϵ of the produced matter and the strength and direction of the collective flow.

  In Figure 12, the distortion of the jet energy distribution is showed for vacuum, static and flowing medium. In the absence of a medium, the parton fragments according to the vacuum distribution. The most important information for our study are changes of the jet shape due to the longitudinal collective flow effects. In the presence of a longitudinal Bjorken-type flow field (hydrodynamics) $u^\mu = (1, \overrightarrow{\beta})/\sqrt{1-\beta^2}$, the longitudinal flow component increases from $T^{zz} = p$ to $T^{zz} = p + \Delta p$, where $T^{\mu\nu}$ is energy-momentum tensor $T^{\mu\nu}(x) = (\epsilon + p)u^\mu u^\nu - pg^{\mu\nu}$, $\Delta p = (\epsilon + p)u^z u^z = 4p\beta^2/(1-\beta^2))$ for the equation of state of an ideal gas, $\epsilon = 3p$. For a rapidity difference $\eta = 0.5, 1.0, 1.5$ between the rest frame, which is longitudinally comoving with the jet and the rest frame of the medium, this corresponds to an increase of the component T^{zz} by a factor 1, 5, 18, respectively. Figure 12 displays marked medium-induced deviation. First, the jet structure broadens because of the medium-induced Brownian motion of the partonic jet fragments in a

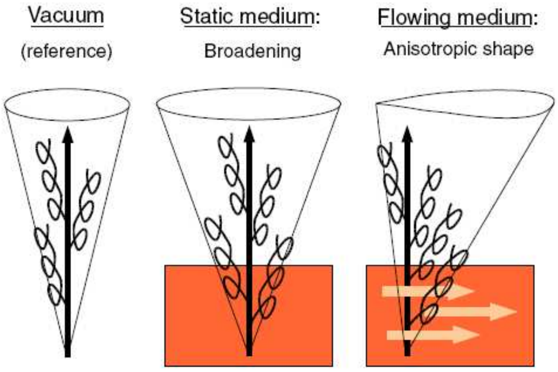

Figure 12: Sketch of the distortion of the jet energy distribution with none, static and flowing medium respectively from left. [26]

dense medium. Second, the jet shape shows rotational assymetry in the $\eta \times \phi$ plane, which is characteristic of the presence of a collective flow field.

In general, the strength of the jet asymmetry due to collective flow effects depends on the (momentum) rapidity difference between the jet and that part of the medium through which the jet propagates. Hence, the rapidity distribution of the jet asymmetry may provide a valuable test of , e.g. hydrodynamical model simulations, which predict deviations form a longitudinally boost-invariant Bjorken expansion of the medium. Events are symmetric with respect to $\eta \rightarrow -\eta$ since the oriented momentum transfer points with equal probability in the positive or negative beam direction respectively. The model calculations were confronted with data of the STAR Collaboration, which measured the widths of the η and ϕ distributions of produced hadrons associated with trigger particles of transverse momentum 4 GeV/c< p_T < 6 GeV/c, which is similar to our study. In Figure 13 are the results - as a function of centrality, the ϕ distribution does not change within errors, while the η distribution shows a significant broadening. Thus, the origin of the angular broadening of jetlike particle correlations is essentially kinematic, being determined by the ratio between the momentum transfer from the medium and the energy of the escaping particle.

To sumarize, according to this model the jet energy distributions and jet-like particle correlations are sensitive to the density of the medium as well as to its collective flow field. This indicates that the energy density produced int the medium can be overestimated significantly if flow effects are ignored. Moreover, the formulation of parton energy loss suggests that partons lose less energy if they escape along trajectories parallel to the transverse flow field. Compared to calculations for a static medium, this enhances the parton energy loss contribution to elliptic flow.

- **Momentum Kick Model** [24]

In the momentum kick model, the near side peak in $\Delta\phi - \Delta\eta$ can be decomposed into a near-side component of the trigger jet and ridge particle component (Figure 10). These two components have very different characteristics. The ridge particles bear the same "fingerprints" as those of inclusive particles, including their particle yields

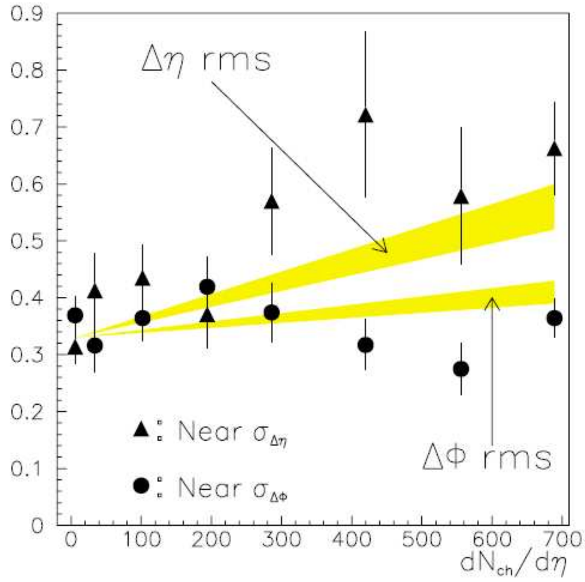

Figure 13: The width in azimuth and rapidity of the nearside distribution of charged hadrons associated with high-p_T trigger particles of transverse momentum 4 GeV/$c < p_T <$ 6 GeV/c in Au+Au collisions at $\sqrt{s_{NN}}$ = 200 GeV. Black points are data from STAR. [26]

increasing with the participant number and their having nearly similar temperatures. These characteristics suggest that the ridge particles originate from the same source as particles produced in the bulk medium.

The $\Delta\phi \sim 0$ correlation of the ridge particles with the trigger jet suggests further that the ridge particles and the jet are related kinematically. The momentum kick model can be then proposed where the ridge particles has been identified as medium partons which suffer a collision with the jet and acquire a momentum kick along the jet direction. After the collided partons materialize as ridge particles and escape from the surface without additional collisions, they retain the collided parton final momentum distribution. The yield of the ridge particles associated with the jet therefore will depend on the momentum kick and the initial momentum distribution of the collided partons before the jet-parton collision.

To gain important insights into the ridge phenomenon, as few as possible parameters is introduced. The relevant quantities are then the magnitude of the momentum kick $\mathbf{q}$ along the jet direction imparted by the jet to the collided parton, and the initial parton momentum distribution represented by the rapidity width parameter σ_y and the transverse momentum temperature $\mathbf{T}$.

While the peak structure along the $\Delta\phi$ direction at $\Delta\phi = 0$ arises predominantly from the momentum kick, the ridge structure along the $\Delta\eta$ direction in the $\Delta\phi - \Delta\eta$ plane on the other hand reflects the initial rapidity distribution dN/dy at the momentum of the jet-parton collision. However, not much is known experimentally about the evolution of the rapidity distribution of partons as a function of time. Momentum kick model simulation for various σ_y and q are plotted in Figure 14.

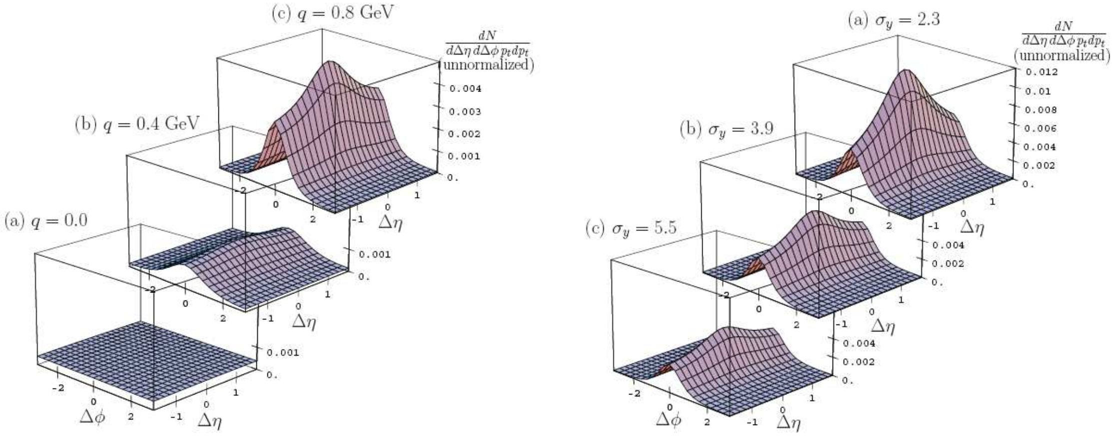

Figure 14: Theoretical results of the momentum kick model of associated ridge particles at $p_T = 2$ GeV as a function of $\Delta\phi$ and $\Delta\eta$. **Left:** (a), (b), (c) are for $q = 0, 0.4, 0.8$ respectively, where q is the momentum kick. **Right:** (a), (b), (c) are for $\sigma_y = 2.3, 2.9, 5.5$ respectively. [24]

- **Medium heating + parton recombination** [28]
  The models suggests that the physics underlying the detail structure of the jet characteristics observed in RHIC experiments can be understood in the framework of parton recombination. Jets produced in heavy-ion collisions create shower partons that are in the environment of thermal partons, which can themselves be enhanced by the passage of hard partons through the medium. That view is common also in another theoretical approaches to the problem. The effort of this method emphasis the recombination model of parton hadronization in the intermediate p_T region. The hadronization formalism is treated in a theoretical way followed by reproducing the real RHIC data that show the existence of peaks in $\Delta\eta$ and $\Delta\phi$ distributions sitting above a flat pedestal and above a broad mount respectively - see Figure 15.

  The general conclusion is that the pedestal in the $\Delta\eta$ distribution can be related to ΔT in the local thermal distribution. No "long-range" correlation has been put in by hand. The pedestal is a consequence of the recombination of the thermal partons among themeselves, which are only indirectly affected by hard scattering through the enhancement of T due to energy loss. Thus the pedestal is not a part of the jet, but cannot be present without it. In the $\Delta\phi$ case, the model predicts functions which fit data in a satisfactory way including the pedestal contribution again using the recombination approach.

- **Radial flow** [25], [40]

  This model describes the heavy-nuclei collisions, where in transverse plane all particles from a single NN collision are initially located at the same position. The subsequent thermalization and transverse radial expansion of the system create strong position-momentum correlations and lead to characteristic rapidity, transverse momentum and azimuthal correlations among the produced particles. The correlations extend over wide rapidity range. Mostly the effect of the transverse radial expansion is discussed. The

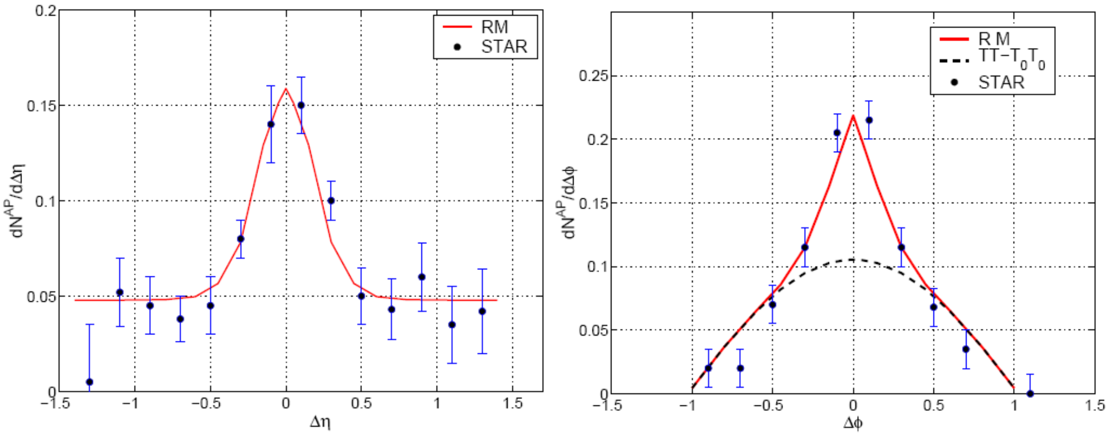

Figure 15: **Left:**Associated particle distribution in $\Delta\eta$ for $2 < p_T < 4$ GeV/c with trigger particle in $4 < p_T^{trig} < 6$ GeV/c. The data are for all charged hadrons in the respective p_T ranges. The solid line is the result of the model's calculation of π^- associated with π^+ trigger. **Right:** Same cuts, distribution in $\Delta\phi$ is shown. The dashed line represents the pedestal effect in $\Delta\phi$ forced to vanish at $|\Delta\phi| = 1$ by the subtraction. [28]

transverse expansion "push" consists of many individual collisions. It leads not only to the increase of the transverse momentum but also to the particle diffusion in the rapidity space. The picture is not boost-invariant, as the initial geometry of the source and particle densities change with rapidity leading to a rapidity dependent radial expansion.

Consequently, the ridge in two-particle correlation function associated with hard trigger at RHIC heavy ion collisions is naturally explained by an interrelation of jet quenching and hydrodynamical transverse flow. The excess particles forming the ridge are produced by QCD bremsstrahlung along the beam (and thus have wide rapidity distribution) and then boosted strongly in radial direction, especially if the $p_T \approx 2$ GeV/c momentum window is selected.

Spectra of particles belonging to a ridge are very different from those of the jet, being much softer. These spectra are completely independent on the jet momentum, which confirms that the ridge is not physically related to a jet itself.

- **Longitudinal broadening of quenched jets in turbulent color field** [27]

This model suggests that the broadening in rapidity during heavy-ion collisions can be explained as the final-state deflection of the gluons radiated from the hard parton inside the medium by soft, transversely oriented, turbulent color fields that arise in the presence of plasma instabilities. The magnitude of the effect is found to grow with medium size and density and diminish with increasing energy of the associated hadron.

The suppression of hadrons is understood to be caused by final-state rescatettering of the leading parton in the dense medium produced in the collision, causing it to lose energy. Within the framework of pertubative QCD, the leading process of energy loss

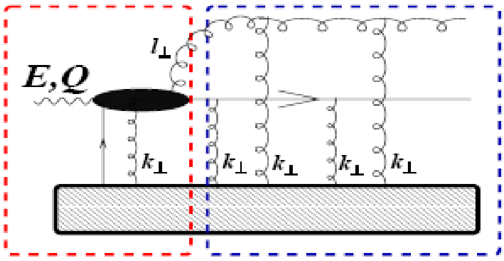

Figure 16: A hard scattering followed by multiple soft rescattering diagram. A jet initiating parton is produced when an incoming light-like parton is struck by a virtual state with forward energy E and virtuality Q^2. The final state parton may be produced off-shell by up to Q^2. [27]

of a fast parton is gluon radiation induced by elastic collisions with color charges in the quasi-thermal medium. Elastic collisions not followed by radiation may also contribute to the energy loss.

Measurement by the STAR collaboration have shown that the leading hadron is accompanied by a cone-shaped pattern of secondary hadrons which are a hard scattered parton. It is called also jet yield. In addition, the trigger parton is observed to be accompanied on the near side by a wide ridge of secondary hadrons, which extends along the beam direction over more than one unit of rapidity in both direction (ridge yield). The energy flow in the ridge-shaped structure grows with participant number and is concentrated in hadrons with transverse momenta $p_T < 2$ GeV/c.

The inclusive yield of associated hadrons receives contributions from the fragmentation of the leading parton as well as from the radiated gluons. The yield of associated hadrons produced in the fragmentation of the hard parton after its exit from the medium is assumed to form the jet yield. This naturally explains why the azimuthal and rapidity distribution of this contribution is identical to that from a jet of the same final energy produced in a $p + p$ collision. Hadrons produced in the fragmentation of the gluons radiated within the medium or after absorption of those gluons is assumed to form the ridge yield. In either case, the ridge shape reflects the kinematic distribution of the radiated gluons at the end of their passage through the medium.

The method proposes also a mechanism of the ridge origin related to the longitudinal expansion of the medium. It builds on the recent insight that extended color fields are dynamically formed in the expanding medium due to the presence of plasma instabilities. Such instabilities have been shown to exist in any quark-gluon plasma with an anisotropic momentum distribution. The nearly boost invariant longitudinal expansion of the matter formed in relativistic heavy ion collisions necessarily induces an oblate momentum distribution of partons with respect to the beam axis. The plasma instabilities lead to the exponential growth of soft modes of the glue field, which ultimately saturate due to the nonlinear self-interaction of the Yang-Mills field, resulting in a turbulent state of the quasi-thermal quark-gluon plasma. The Fields will most strongly affect those gluons which carry a small fraction of the jet's longitudinal momentum (with short formation time) and are emitted at a substantial angle with respect to the jet axis. A sketch with a hard scattering event with induced radiation is in Figure 16.

2 Experimental Setup

2.1 RHIC Accelerator

The Relativistic Heavy-Ion Collider (RHIC) is located at Brookhaven National Laboratory (BNL) on Long Island, New York. It is the largest collider capable of heavy-ion collisions in the world. RHIC was designed to collide heavy ions at center-of-mass (CMS) energy of up to 200GeV per colliding nucleon pair. The central focus of the RHIC physics program is study of nuclear matter at high temperatures and densities. In the central collision of the ultra-relativistic nuclei, enormous energy densities ($>$1GeV/fm^3) are created. These conditions may create a system of the the theoretically proposed state of deconfined quarks and gluons - the Quark Gluon Plasma (QGP). This system expands rapidly and hadronizes. Particles are then able to be detected. The program is also focused on polarized protons.

The RHIC storage ring is 3.83 km long with six designed interaction points. There are two large detector systems (i.e. experiments) - STAR (6 o'clock), PHENIX (8 o'clock) and two small ones - PHOBOS (10 o'clock), BRAHMS (2 o'clock).

For Au+Au relativistic collisions, the Au ions must be accelerated first. RHIC uses accelerating chain showed in Figure 17. Up to 112 particle bunches per ring can be injected, whereas the time between bunch crossing at the interaction points is 106 ns. The design luminosity for Au+Au collisions is 2×10^{26}cm^{-2}s^{-1}. Collisions of asymmetric species, i.e. different kinds of particles in the two beams, is also possible due to independent rings with independent steering magnets. The first physics run took place in 2000 after almost ten years of development. First colliding particles were Au+Au collisions at 130 GeV per nucleon. The following four running periods included Au+Au collisions at 200, 62.4 and 19.6 GeV/A, Cu+Cu collisions at 200, 62.4 and 22.4 GeV/A, d+Au collisions at 200 GeV/A and polarized p+p collisions at 200 GeV.

For Au beam operations, the Au ions with charge Q = -1e are created using the **Pulsed Sputter Ion Source.** Then they are accelerated through the **Tandem Van de Graaf facility** and a series of stripping foils. The Au ions at the exit are at the kinetic energy of 1 MeV/A and a net charge of Q = +32e. The ions are then injected into the **Booster Synchrotron** and accelerated to an energy of 95 MeV/A. After the Au ions leave the booster, they are further stripped to Q = +77e and transferred into the **Alternating Gradient Synchrotron (AGS)**, where they are accelerated to 8.86 Gev/A and sorted into four final bunches. Finally, the ions are injected into RHIC and stripped to the bare charge state of Q = +79e during the transfer. For *pp* operations, protons are injected from the 200 MeV **Linac** into Booster and then the procedure is the same.

2.2 STAR detector overview

The Solenoidal Tracker at RHIC (STAR) is one of the two large experiments at BNL . The STAR was designed to have a large acceptance (including full 2π azimuthal acceptance), high precision tracking, momentum determination and particle identification [5].

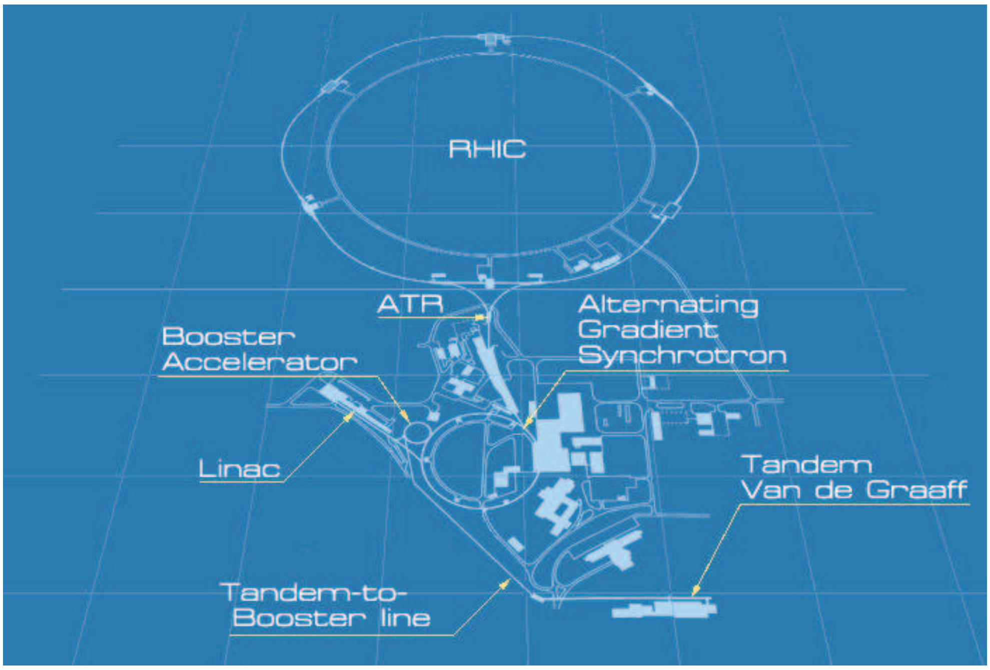

Figure 17: Schematics of the RHIC accelerating chain.[www.bnl.gov]

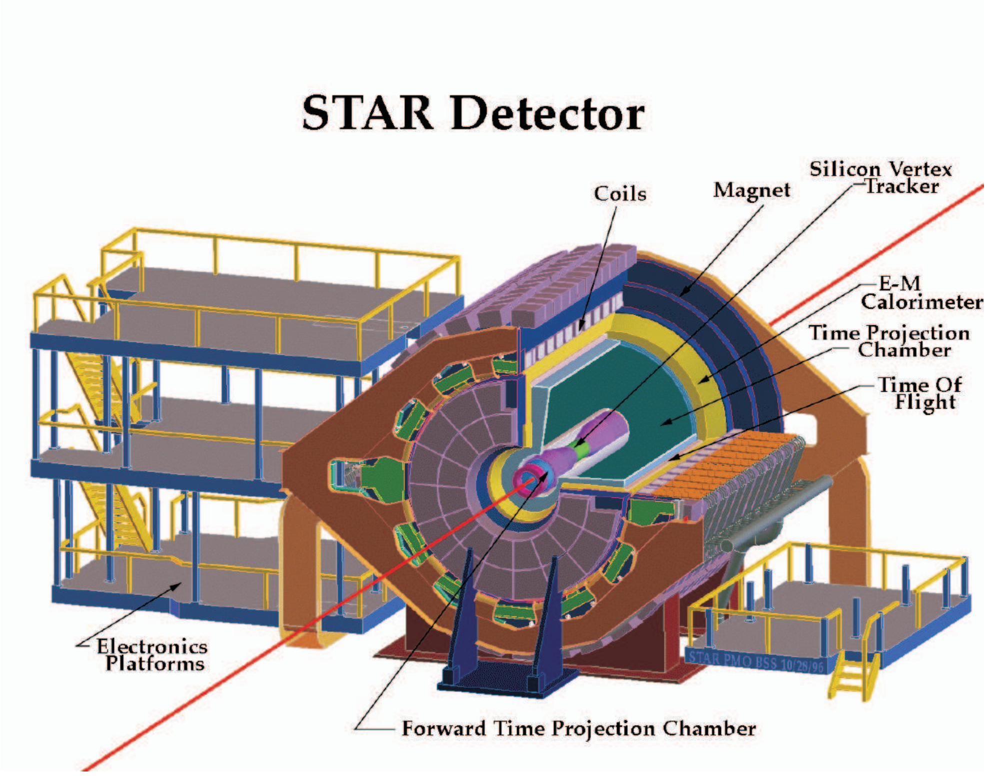

Figure 18: Isometric view of the STAR detector. [5]

The whole detector is surrounded by a **solenoidal magnet** 0.5T of intensity (See Figure 18) [6]. The magnet allows determination of particles due to the particle's paths curvatures. The beam pipe is surrounded by a three layer **Silicon Vertex Tracker (SVT)** [7], followed by an additional layer of **Silicon Strip Detector (SSD)** [8]. These detectors cover full azimuthal angle and also $|\eta| < 1$ in pseudorapidity. The SVT and SSD enhanced the measurement of hadrons with a short lifetime by providing detailed inner tracking. The main subdetector, and the heart of the STAR itself, is a large volume **Time Projection Chamber (TPC)** [9], which provides primary tracking of charged particles and its identification via energy loss. The TPC has full azimuthal coverage and $|\eta| < 1.8$ in pseudorapidity. Furthermore, particles may be tracked in forward direction (large $2.7 < |\eta| < 3.9$) using two **Forward Time Projection Chambers (FTPC)** [13]. More details about TPC can be found in the following section. To extend particle identification, **Time of Flight (TOF)** detector is also used in STAR. There are two ElectroMagnetic calorimeters (EMC) at STAR. These allow measuring of transverse energy and also useful for triggering on high p_T photons, electrons and electromagnetically decaying hadrons. The two EMCs are the **Barrel EMC** [14] and **Endcap EMC** [16]. The first one surrounds the TPC, while the latter is in front of the TPC. These EMCs provide full azimuthal coverage for the combined pseudorapidity of $-1 < \eta < 2$. There are another additional detectors used for triggering. **The Central Trigger Barrel (CBT)**, **Zero-Degree Calorimeters (ZDC)** and **the Beam Beam Counters (BBC)**.

For further study of the STAR technical details, we recommend the official publication in Nucluclear Instruments and Methods A 499 (2003). Corresponding bibliography items are [5]-[16].

2.2.1 STAR Time Projection Chamber (TPC)

[9] The STAR TPC is the central element in a suite of detectors that surrounds the interaction vertex. It is used for recording tracks of particles, measures their momenta and identifies the particles by measuring their ionization energy loss (dE/dx). Its acceptance covers $|\eta| < 1.8$ units of pseudorapidity through the full azimuthal angle. Particles are identified over a momentum range from 100 MeV/c to 30 GeV/c.

The STAR TPC is shown schematically in Figure 19. It sits in a large solenoidal magnet that operates at 0.5 T. The TPC is 4.2 m long and 4 m in diameter. It is an empty volume of $P10$ gas in a well-defined, uniform electric field of ~ 135 V/cm. The paths of primary ionizing particles passing through the gas volume are reconstructed with high precision from the released secondary electrons which drift to the readout endcaps at the ends of the chamber. The uniform electric field which is required to drift the electrons is defined by a thin conductive Central Membrane (28 kV) at the center of the TPC, concentric field-cage cylinders and the readout endcaps (grounded). Electric field uniformity is critical since track reconstruction precision is submilimeter and electron drift paths are up to 2.1 m.

The readout system is based on Multi-Wire Proportional Chambers (MWPC) with readout pads. The avalanche amplification on anode wires is $1000 - 3000$. The induced charge from an avalanche is shared over several adjacent pads and the original track position can be reconstructed to a small fraction of a pad width. There are a total of 136608 pads in the readout system. The readout modules, or sectors, are arranged as on a clock with 12 sectors around circle. The modular design with manageable size sectors simplifies construction and

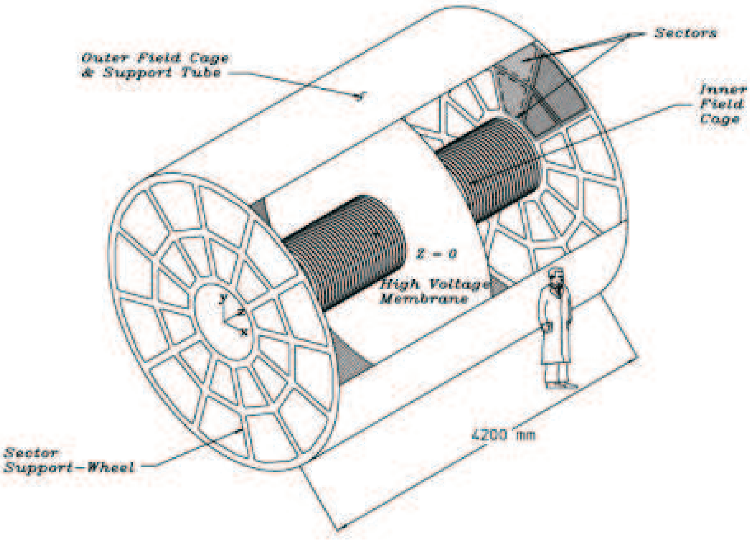

Figure 19: The STAR TPC surrounding the beam pipe. The collisions take place near the center of the TPC.[9]

maintenance. There are only 3 mm spaces between the sectors to keep blind places as small as possible. One sector can be seen in Figure 20.

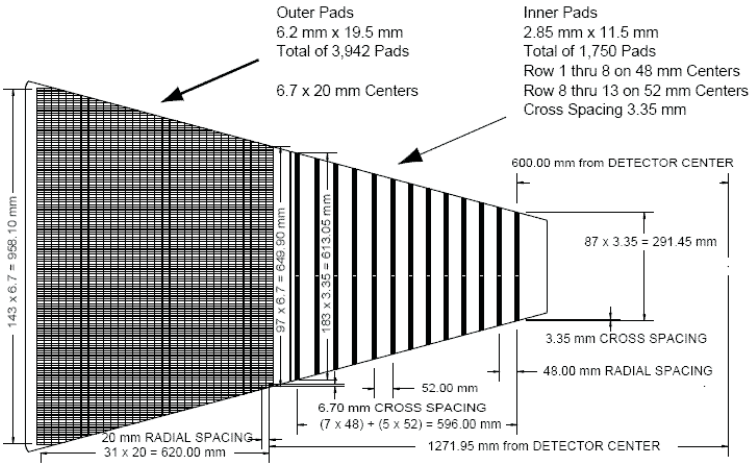

Figure 20: The anode pad plane with one full sector shown. The inner subsector is on the right and it has small pads arranged in widely spaced rows. The outer subsector is on the left and it is densely packed with larger pads [9].

Concerning the $P10$ gas inside the TPC, is consists of 10% methane and 90% argon regulated at 2 mbar above atmospheric pressure. Its primary attribute is a fast drift velocity which peaks at a low electric field. The important condition is constant drift velocity, insensitive to small variation in temperature and pressure. This also requires keeping oxygen intoxication below 100 parts per million and water less than 10 parts per million.

Energy loss in the TPC gas is a valuable tool for identifying particle species. It works especially well for low momentum particles but as the particle energy rises, the energy loss becomes less mass dependent and it is hard to separate particles with velocities $v > 0.7$c. STAR was designed to be able to separate pions and protons up to 1.2 GeV/c. this requires a relative dE/dx resolution of 7%. So the challenge is to calibrate the TPC and understand the signal and gain variations well enough to be able to achieve this goal.

The measured dE/dx resolution depends on the gas gain which itself depends on the pressure in the TPC. The readout electronics also introduce uncertainties in the dE/dx signals. There are small variations between pads, and groups of pads, due to the different response of each readout board.

Therefore, it is not possible to accurately measure the average dE/dx. Instead, the most probable energy loss is measured and fitting the dE/dx distribution including all clusters associated to a given tracs was found to be more effective. Figure 21 shows the energy loss of for particles int the TPC as a funciton of the particle momentum. This picture includes both primary and secondary particles.

To sum up, the STAR TPC is more than sufficient for tracking and identification of charged particles. In this work, it is the main detector used for analysis.

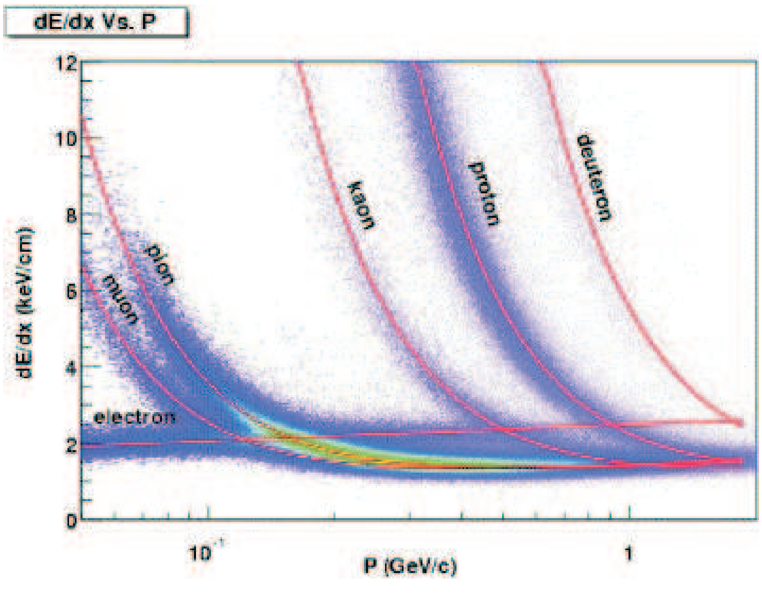

Figure 21: The energy loss distribution for primary and secondary particles in the STAR TPC as a function of the p_T of the primary particle (magn. field was 0.25 T). The convergency towards higher p_T is obvious - so the particle distinguishing is quite not possible.[9]

3 Analysis

The necessary theoretical framework has been presented in previous sections. Therefore it is appropriate to challenge the theoretical ideas with real data from the STAR experiment.

The first step is to treat the detector tracking efficiency via pion embedding. Then, the data can be studied further. As the raw data bring too much information and it is impossible to distinguish the important effects from background, they must be filtered in some way. To subtract the background, several subsequent steps are used. The largest contribution is from non-physical effects, which are eliminated via mixing events (or also called combinatorial background). Next, the elliptic flow and contribution from soft and hard processes are taken into consideration.

3.1 Event and Particle Track Selection

Data from the Run4 (2004-2005) measured by the STAR experiment were used for this analysis. The data sample contains 49 millions Au+Au collisions at $\sqrt{s_{NN}} = 200$ GeV. For the analysis, we have used following event selection criteria: z-coordinate of the interaction vertex v_z was selected to be $|v_z| < 30$ cm, the trigger identification number was 15007 (minimum bias trigger) and 15105 (12% central cut on ZDC, details can be found on the STAR trigger webpage [41]). The charged tracks selection criteria are: number of hits which are fit on the track in the TPC is ≥ 15, minimum p_T of the track is 1 GeV/c, $|\eta| < 1$, the magnitude of the distance of the closest approach (DCA) to the primary vertex was set to be less than 1 cm. The data were produced using the STAR software library SL05b and SL05c.

Both minimum bias and online central-triggered data can be subdivided into centrality classes after event reconstruction. Offline centrality selection is achieved by selecting events

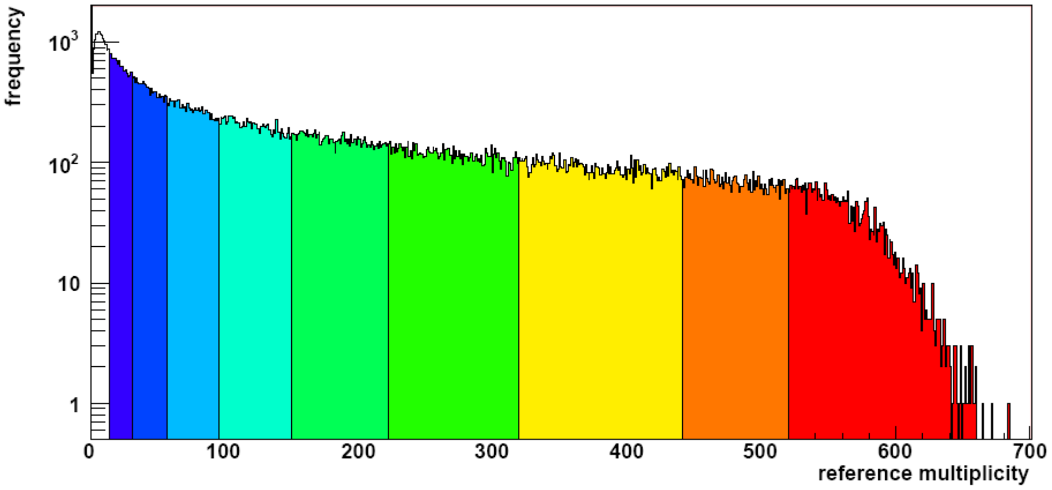

Figure 22: Reference multiplicity distribution for offline centrality definition, in Au+Au collisions at $\sqrt{s_{NN}} = 200$ GeV. Fill colour represents centrality class. From red to blue: 0-5%, 5-10%, 10-20%, 20-30%, 30-40%, 40-50%, 50-60%, 60-70%, 70-80%.

Bin	Centrality	$\mathbf{N_{part}}$	$\mathbf{N_{bin}}$	$\mathbf{N_{ch}}$
1	0-5%	352.4 +3.4 -4.0	1051.3 + 71.5 -71.1	520
2	5-10%	299.3 +6.6 -6.7	827.9 +63.9 -66.7	441
3	10-20%	234.6 +8.3 -9.3	591.3 +51.9 -59.9	319
4	20-30%	166.7 +9.0 -10.6	368.6 +41.1 -50.6	222
5	30-40%	115.5 +8.7 -11.2	220.2 +30.0 -38.3	150
6	40-50%	76.6 +8.5 -10.4	123.4 +22.7 -27.3	96
7	50-60%	47.8 +7.6 -9.5	63.9 +14.1 -18.9	57
8	60-80%	20.9 +5.1 -6.5	21.2 +6.6 -7.9	14

Table 1: Centrality definition. Each centrality bin is defined by fraction of geometric cross-section, number of participating nucleons N_{part}, number of inelastic binary nucleon-nucleon collisions N_{bin} and primary charged track multiplicity N_{ch} in the TPC $|\eta| < 0.5$.

within ranges of reconstructed track multiplicity. In order to avoid variations in tracking efficiency as a function of primary vertex position, a reference multiplicity is used, which only includes tracks with pseudo-rapidity $|\eta| < 0.5$. A typical reference multiplicity distribution for minimum bias Au + Au collisions at $\sqrt{s_{NN}}$ = 200 GeV is shown in Figure 22, with centrality classes indicated by fill colour. Glauber model Monte Carlo calculations [35] are used to relate centrality to the number of participants, impact parameter, number of binary collisions etc.

Our analysis is done for various centrality bins defined in Table 1. Each bin is characterized by fraction of geometric cross section, number of participants, number of binary collisions and measured primary charged track multiplicity in the TPC within $|\eta| < 0.5$.

3.2 Detector Track Reconstruction Efficiency Correction

Every detector reconstructs tracks with different and finite efficiency. Particles that penetrate an active detector volume may still not be correctly reconstructed. This can be caused by dead channels in detector, space-charge distortions, merging of tracks, fake tracks etc. It is also caused by the detector sensitivity to specific momentum and angular magnitude. For example, TPC has very low track detection efficiency in low p_T region.

The best way to deal with this issue is to analyze known signal in the real event environment since it almost impossible to simulate whole event. In fact, charged pions are generated in full kinematic range of interest and then embedded into real event. Then, these pions are run through the full analysis chain to see if the input signal was reconstructed correctly. Generally, the efficiency can be written down as a portion of input and output signal obtained

$$\varepsilon(p_T, \eta, centrality) = \frac{OutputSignal}{InputSignal} \tag{5}$$

In STAR, the pions are produced in Monte Carlo simulation and then reconstructed using GEANT software. This simulate the interaction between particle and detector material. The STAR virtual detector is constructed in GEANT and every Monte-Carlo generated particle passes through all its elements taking into account all the material, multiple scattering, energy loss, conversions and particle decays. The final Output is the complete information of the particle's trajectory and interactions in the active detector volumes.

These signals are then **embedded** to real event and such modified event is processed using the standard analysis chain from STAR. The Output signal therefore carries the same efficiency pattern as the real data. Using the formula (5), the real detector track reconstruction efficiency is obtained. As the analysis is CPU consuming, the embedded events are centrally generated and then distributed to collaboration members.

Every particle (or track) recorded from real event must be corrected by this detector efficiency in order to keep the original distribution of particles preserved. In fact, it means weighting every recorded particle by $1/\varepsilon$. To get these weighting parameters, which depend on p_T, pseudorapidity η and centrality, the correction function must be derived. It is obtained by fitting the efficiency as a function of p_T and η data for every centrality bin. As a fit function of p_T, the most suitable is the **ArcTangent** function, since the efficiency is also limited by the unity (of probability) from above. Moreover, we are not interested in the very low transverse momentum region, where the additional restrains must be applied. The p_T efficiency and the fit ArcTan are shown in Figure 23-left and they smoothly follow the data in region from 0.3 GeV/c to 5 GeV/c, extrapolated to 6 GeV/c for our purposes with χ^2 far below 1. The same procedure can be applied also for pseudorapidity efficiency distribution. The efficiency is almost flat in pseudorapidity and steeply falls at the edges of the TPC acceptance, and can be easily fit by a polynomial function even in powers due to the left/right symmetry (Figure 23-right). As the reconstruction efficiency is both p_T and η dependent, two dimensional correction function is needed. That can be obtained by fitting the $\eta \times p_T$ efficiency distribution. It is assumed that the p_T is not dependent on η in our scale, so the function will not contain any mixed $\eta \times p_T$ component.

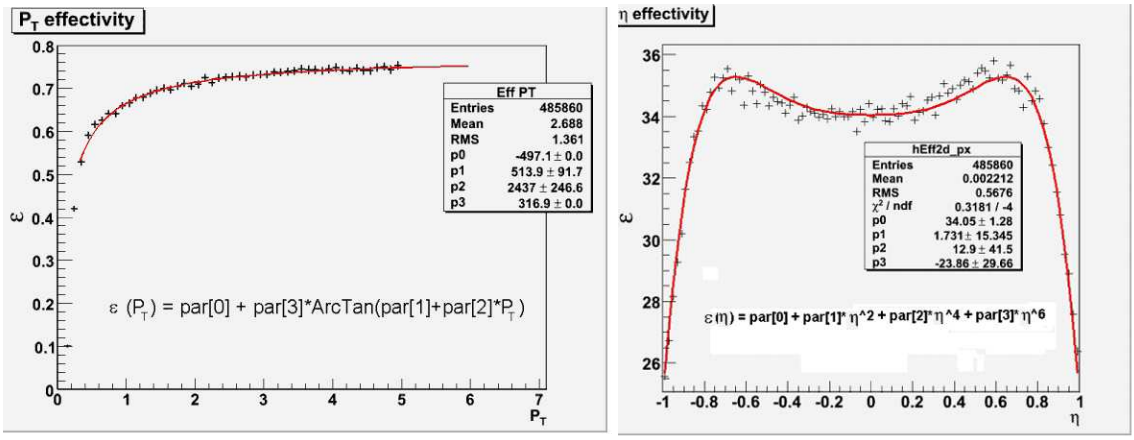

Figure 23: **Left:** Fit p_T efficiency (according to (5)) by ArcTangens function from 0.3 GeV/c to 6 GeV/c. **Right:** Fit η efficiency in TPC acceptance region by polynomial function in even powers. Both pictures are in 0-5% centrality.

The resulting correction function is in a form

$$\varepsilon(\eta, p_T) = par[0] + par[3] * ArcTan(par[1] + par[2] * p_T) + par[4] * \eta^2 + par[5] * \eta^4 + par[6] * \eta^6 \quad (6)$$

and its shape, together with the efficiency data, is shown in Figure 24. Fit parameters are summarized in Table 2.

The difference between the ε from the embedded data and the fit function given by Eq.(6) are shown in Figure 25. In the p_T range relevant for this thesis ($p_T > 1\mathrm{GeV}/c$) they agree within 1%.

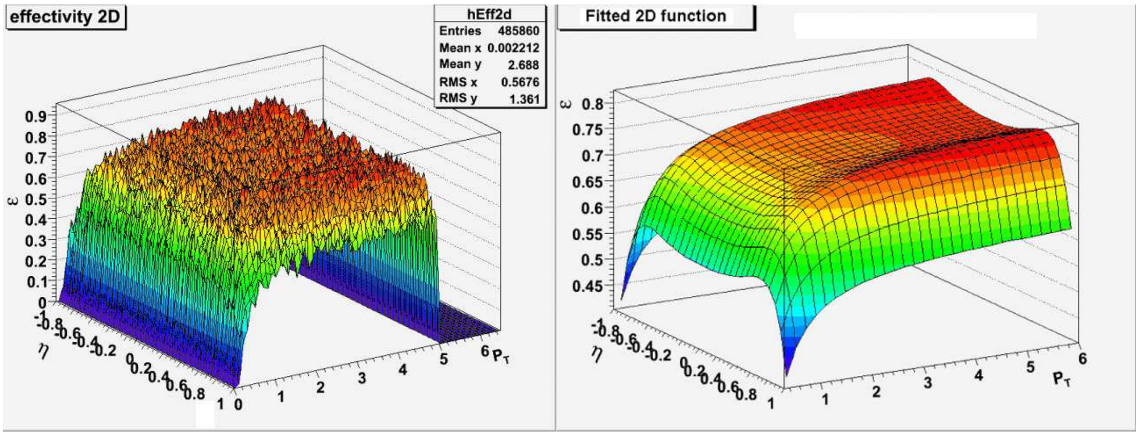

Figure 24: Detector track reconstruction efficiency as a function of p_T and η. **Left:** Data, **Right:** fit function (6). Both pictures are in 0-5% centrality.

Params	**0-5%**	**5-10%**	**10-20%**	**20-30%**	**30-40%**
par[0]	-3510.50	-21.74	-5913.77	-3394.13	-4933.60
par[1]	3362.99	27.54	8588.11	5538.02	11887.22
par[2]	17267.70	106.34	30029.40	19668.58	22544.86
par[3]	2235.35	14.35	3765.35	2161.30	3141.37
par[4]	0.0380	0.0694	0.0114	0.0114	-0.0257
par[5]	0.2812	0.1308	0.2523	0.2358	0.3108
par[6]	-0.5133	-0.3855	-0.4551	-0.4505	-0.4926
Params	**40-50%**	**50-60%**	**60-70%**	**70-80%**	**80%+**
par[0]	-371.41	-7830.61	-84.36	0.7350	-0.9307
par[1]	1006.10	25151.51	303.01	-0.5038	5.5317
par[2]	1662.81	28957.11	226.42	0.7543	3.3585
par[3]	237.00	4985.68	54.27	0.0757	1.1204
par[4]	-0.0018	-0.0275	-0.0411	0.0781	0.1386
par[5]	0.2095	0.2773	0.3070	-0.0129	-0.0290
par[6]	-0.4147	-0.4556	-0.4893	-0.2752	-0.2844

Table 2: Fit parameters for the TPC track efficiency function Eq.(6) as a function of centrality.

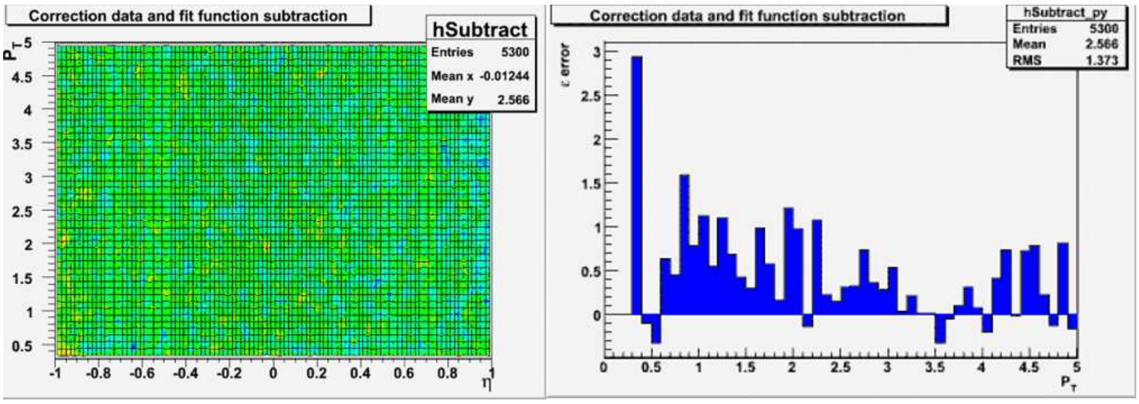

Figure 25: **Left:** Subtracted efficiency data and our fitting function. **Right:** Projection of subtracted efficiency into p_T. We are not concerned by the low p_T error since we are not interested in this low p_T region.

3.3 Three-Particle Correlation Analysis Method

The three-particle correlation analysis is made on an event by event basis using ROOT framework [42]. It means that each collision is analyzed separately. Charged particles in each event are stored in Particle list and then processed. First, an event containing at least one trigger particle with transverse momentum 3 GeV/c $< p_T^{trig} <$ 6 GeV/c is identified. Then, in this specific event, the particle list is looped over from the beginning again to look for associated particles which satisfy the condition 2 GeV $< p_T^{assoc} < p_T^{trig}$. Every combination of one trigger and two associated particles enters into the correlation function defined as

$$C(\Delta\eta_1, \Delta\eta_2) = \frac{1}{N_{trig}} \frac{dN_{pair1}}{d(\Delta\eta_1)} \frac{dN_{pair2}}{d(\Delta\eta_2)} \frac{1}{\varepsilon_1^{assoc}} \frac{1}{\varepsilon_2^{assoc}} \tag{7}$$

where N_{trig} is the number of trigger particles and $\Delta\eta_1 = \eta^{trig} - \eta_1^{assoc}$, $\Delta\eta_2 = \eta^{trig} - \eta_2^{assoc}$ are angles between the trigger particle and the first associated particle and the trigger particle and the second associated particle respectively. The correlation function is also corrected for finite track reconstruction efficiency of associated particles ε_1^{assoc} and ε_2^{assoc} given by Eq.(6). When all the possible sets of two associated particles are assigned to the trigger, the loop algorithm continues through the Particle list and searches for another trigger particle which fulfills the above mentioned momentum cut. To this trigger again, the search for associated particle pairs is repeated. As it cannot be distinguished which of the two associated particles is "the first" and which is "the second", both combinations are mirrored in the data plot and, in fact, recorded twice.

In order to focus only on the ridge region, the near-side peak $|\Delta\phi| < 1$ rad is selected from the full two-particle azimuthal distribution, where $\Delta\phi = \phi^{trig} - \phi^{assoc}$.

3.4 Detector Acceptance Corrections

Another effect which has to be taken into account before the final data interpretation can be made is the finite detector acceptance. This effect was found to be the same in every event recorded during the data taking which enables to eliminate them in a systematic way. Commonly used method for dealing with this issue is mixed event technique which is based on correlating particles from independent events. In this way, all the physics correlations cancel out and only the detector acceptance issues remain.

In the experimental setup section 2.2.1, the STAR TPC was introduced and it was pointed out, that it has an **azimuthal structure** because of the 12 radial sectors and gaps (Figure 20). These gaps affect the possible reconstructed ϕ, and consequently $\Delta\phi$ values. To demonstrate this effect, in Figure 26-left is plotted the ϕ distribution of the first associated particles. The 12 sector gaps are clearly visible. The same pattern is visible for each set of particles. From these ϕ distributions a trigger particle is randomly selected and correlated with a random associated particle (which has its own ϕ distribution, however with the same gaps pattern). The resulting mixing histogram for $\Delta\phi$ is obtained (Figure 26-right). All mixing histograms are normalized to unity and corrected to detector track efficiency in p_T and η (if applicable).

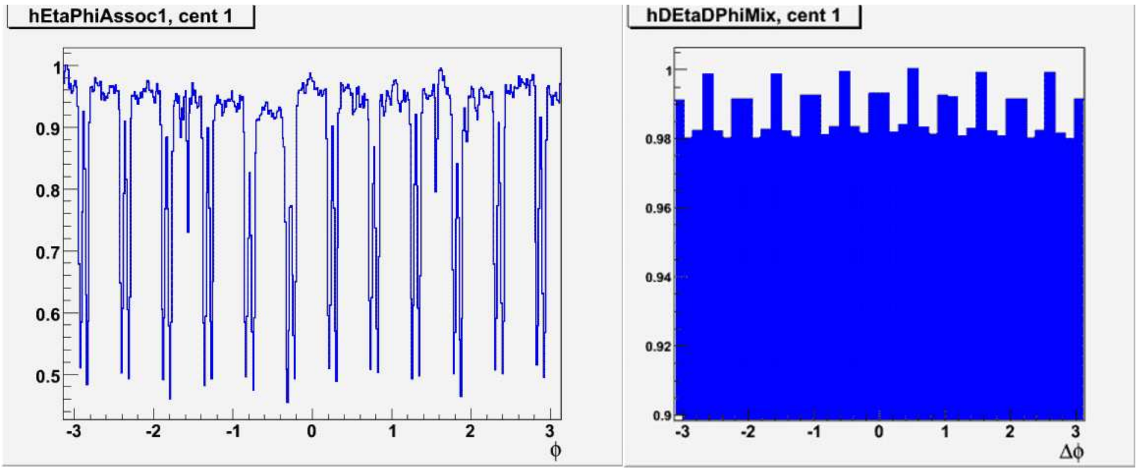

Figure 26: **Left:** ϕ acceptance of charged tracks in the TPC. 12 sector gaps are clearly identified. **Right:** Azimuthal difference $\Delta\phi$ resulting from mixing random trigger and (first) associated particle. More details are in text.

The pseudorapidity (η) acceptance of the TPC is uniform in $-1 < \eta < 1$. Combining two uniform η distributions of trigger and associated particle will result in a triangular shape as demonstrated in Figure 27. It is a pure combinatorial result. If we extend our study to $\Delta\eta_1 \times \Delta\eta_2$ space, ie. combine two triangular distributions, the resulting acceptance pattern is a hexagonal-shape pyramid shown in Figure 28.

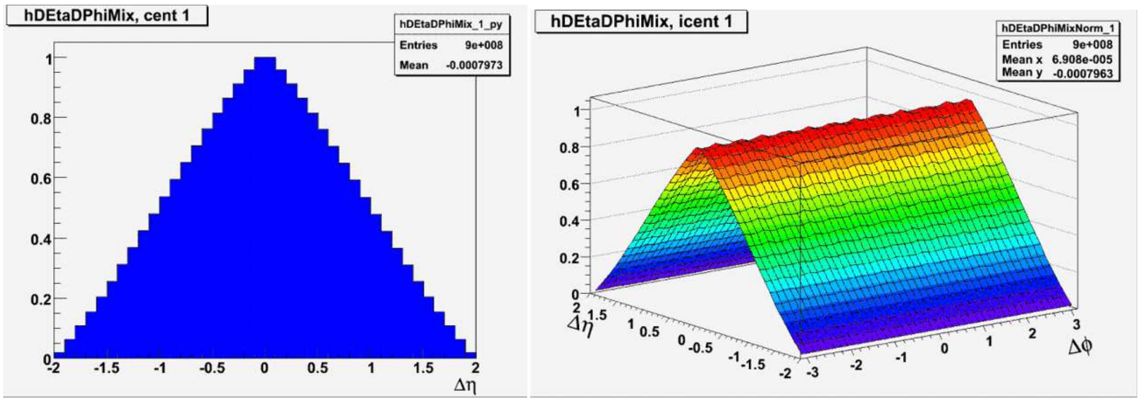

Figure 27: **Left:**$\Delta\eta = \eta^{trig} - \eta_1^{assoc}$ acceptance acquired by combining random trigger and random associated particle correlations. **Right:** $\Delta\phi \times \Delta\eta$ acceptance correction.

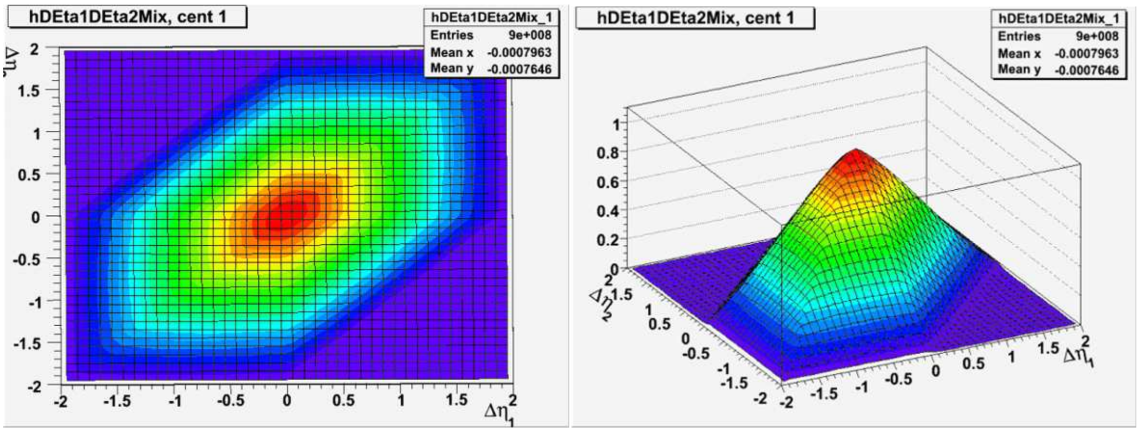

Figure 28: $\Delta\eta_1 \times \Delta\eta_2$ acceptance acquired by combining two mixed events, which form $\Delta\eta_1$ and $\Delta\eta_2$ distributions.

4 Results

4.1 Two-Particle Correlations

The two-particle correlations are defined by correlation function

$$C(\Delta\phi, \Delta\eta) = \frac{1}{N_{trig}} \frac{d^2 N_{pair}}{d(\Delta\phi) d(\Delta\phi)} \frac{1}{\varepsilon^{assoc}}, \tag{8}$$

where N_{trig} is the number of trigger particles and $\Delta\eta = \eta^{trig} - \eta^{assoc}$, $\Delta\phi = \phi^{trig} - \phi^{assoc}$ are angles between the trigger particle and the associated particle. The correlation function also includes correction for the track reconstruction efficiency of the reconstructed particle.

The measured correlation function is displayed in Figure 29-left. In our analysis, to every trigger particle satisfying 3 GeV/c $< p_T^{trig} <$6 GeV/c is assigned an associated particle from the same event in momentum range of 2 GeV/c $< p_T^{assoc} < p_T^{trig}$. The near side peak is still observable in the presence of significant background. Even the ridge contribution remains visible.

Dividing the correlation Eq.(9) by the 2-particle mixed event correction (Figure 27), the clear two-particle correlation is obtained (Figure 29-right). Near-side peak is deformed along $\Delta\eta$ projection and forms the ridge structure. In the place of the away-side peak ($\Delta\phi \approx \pi$), no explicit shape is formed, greatly overwhelmed by the elliptic flow contribution.

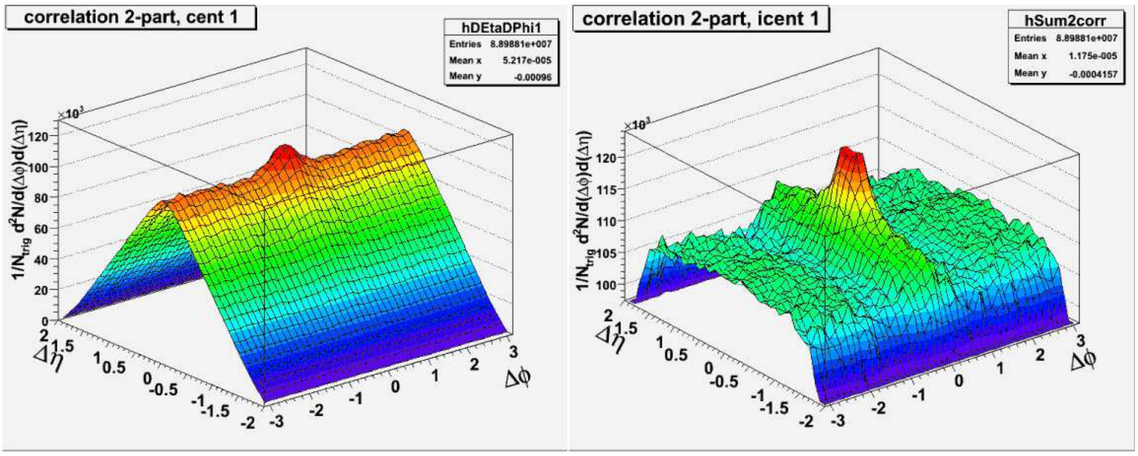

Figure 29: **Left:** Two-particle raw data correction with all background. **Right:** Two-particle correlation with applied mixed event correction.

4.1.1 Elliptic Flow and Background Subtraction

Jet-like correlations are not the only correlations in the event. The azimuthal particle distribution in two particle correlations is described by the equation (4). It means that particles are affected by elliptic flow v_2, which gives rise to a $cos(2\Delta\phi)$ modulation of the background. This is subtracted by using Zero Yield at 1 radian (ZYA1) method, which suppose no jet yield at $|\Delta\phi| \approx 1$ [31]. Therefore, the functional form of the background is

$$C(\Delta\phi, p_T) = B(1 + 2v_2(p_T^{trig})v_2(p_T^{assoc})cos(2\Delta\phi)) \tag{9}$$

The parameter **B** is obtained by averaging the bin value at $|\Delta\phi| \approx 1$. Consequently, the flow contribution is plotted using (9) into Figure 30.

Figure 31 shows two-particle correlation with elliptic flow contribution subtracted. $\Delta\eta$ correlation without v_2 is also shown. Particulary, the near-side peak is clearly visible and with correspondence to the p+p and d+Au $\Delta\phi$ distributions in Figure 9. The away-side peak is modificated and has a double hump structure which can be explained by existence of the Mach cone created by the passing particle through the hot and dense matter [33]. If the speed of sound is 1/3 of the speed of light, the Mach cone angle would create a maximum at $\pi - 1.2$ rad, which corresponds to $\Delta\phi \approx 1.9$. This also also in agreement with our result.

v_2 values were taken from the official STAR source [www.star.bnl.gov], which takes the mean v_2 value obtained by "modified reaction plane method" method ($v_2\{RP\}$) and the four particle cumulant method ($v_2\{4\}$). The correlation yields are corrected for the centrality dependence and are normalized per bin and number of trigger particles. Background is constructed from mixing event technique.

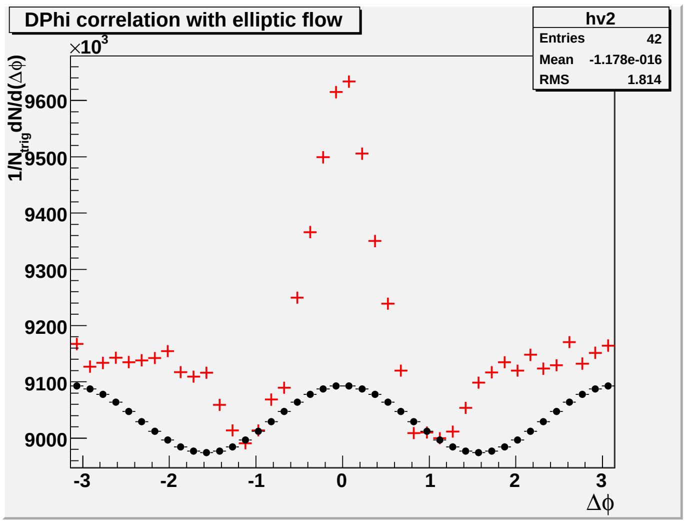

Figure 30: Two particle correlation data (red) with errors plotted along with the v_2 modulated background obtained by ZYA1 method (black circles).

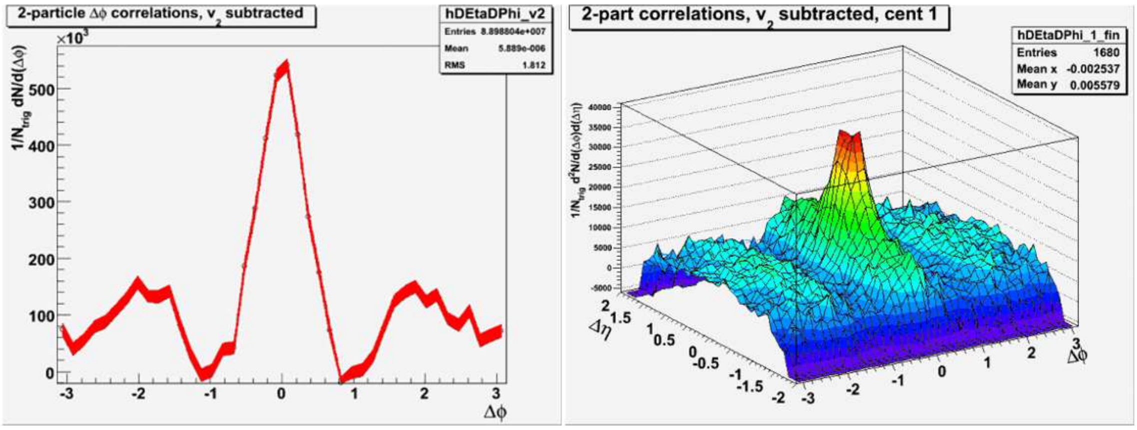

Figure 31: **Left:** $\Delta\phi$ two-particle correlation with subtracted elliptic flow, "Mach cone pattern" is visible on the away side. The errors are displayed by the red band. **Right** $\Delta\phi \times \Delta\eta$ two-particle correlation with subtracted elliptic flow.

4.2 Three-Particle Correlation

Dividing the correlation function Eq.(8) (plotted in Figure 32-left) by the mixed event acceptance correction (Figure 28) it is eventually possible to investigate the features of the measured three-particle correlations. Contrary to two-particle correlations where the near side peak and partly the ridge structure can be distinguished in non corrected data (Figure 29-left), in three-particle correlations the structure appears only after the mixed event correction.

The resulting correlation histogram is presented in Figure 32-right. We can notice several distinct patterns on the top of the huge background pedestal which has been suppressed on purpose in order to make visible the weak correlation.

The most visible feature of the correlation in Figure 32-right is the (near-side) peak in

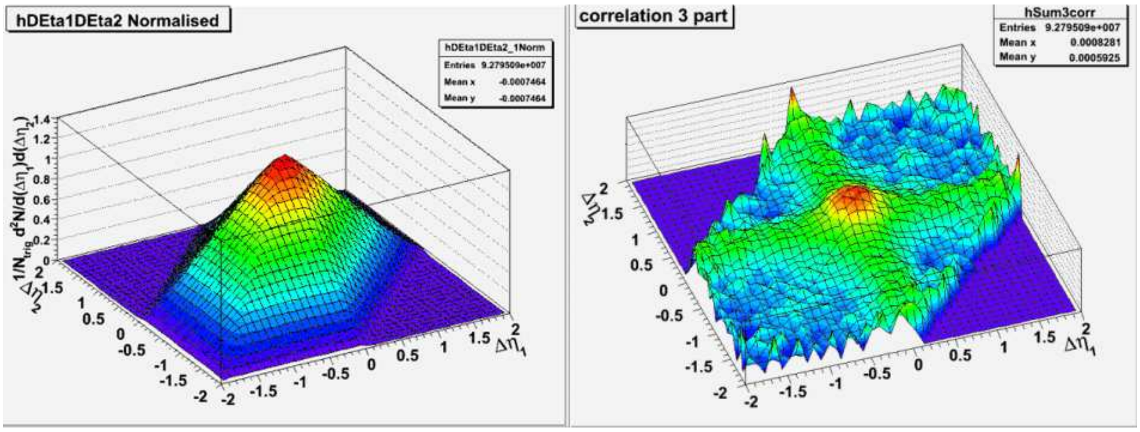

Figure 32: $\Delta\eta_1 \times \Delta\eta_2$ correlation. **Left:** Raw data obtained from STAR experiment. **Right:** Raw data divided by mixing histogram (acceptance) from Figure 28 (zoomed picture). Both pictures in the first centrality bin.

the middle, corresponding to $\Delta\eta_1 \approx \Delta\eta_2 \approx 0$. The second most visible pattern is the *cross*. It originates from the residual correlation as the most particles are in the jet component. It means, that the first particle has the largest probability to be in the closest vicinity to the trigger particle, ie. $\Delta\eta_1 \approx 0$. The second particle is then distributed across the whole acceptance according to correlation pattern under condition being studied. As all the particles are mirrored, ie. recorded twice, the pattern is symmetric along the diagonal. Figure 33 demonstrates the evolution of the three-particle correlations with centrality.

4.2.1 Elliptic Flow and Background Subtraction

Then, the analysis follow the method suggested by J. Ulery and F. Wang for three-particle correlations [32]. In that case, there are two sources of background. First, referred as Hard-Soft (HS), is obtained when one of the two associated particles is correlated with the trigger and the second associated particles is randomly chosen from other event (TA+A). Second, referred as Soft-Soft (SS), neither of the two associated particles is correlated with the trigger particle, but they are correlated with each other (T+AA).

As a whole, the resulting signal can be formulated as

$$\begin{aligned} S(\Delta\eta_1) \otimes S(\Delta\eta_2) = \quad & Raw(\Delta\eta_1) \otimes Raw(\Delta\eta_2) \\ & -[Bckg(\Delta\eta_1) \otimes Bckg(\Delta\eta_2)]_{SS} \\ & -[Raw(\Delta\eta_1) \otimes Bckg(\Delta\eta_2) + Raw(\Delta\eta_2) \otimes Bckg(\Delta\eta_1)]_{HS} \end{aligned} \tag{10}$$

Hard-Soft contribution for Trigger+Assoc1 (correlated) with one random Assoc2 (inputed) from another event are plotted in Figure 34. Hard-Soft contribution eliminates the significant cross in $\Delta\eta_1 \approx 0$ and $\Delta\eta_2 \approx 0$, while the Soft-Soft contribution in more evenly distributed (Figure 35) except the diagonal. That is why the SS background must be treated with care in order not to destroy possible present $\Delta\eta_1 \approx \Delta\eta_2$ correlations.

If this background effects are to be subtracted from data using (10), it is necessary to correct the HS and SS to flow contributions since the correlation effects are of the same magnitude as the flow from the background. It includes many parameters, including v_2 and even v_4 flow. The whole parametrization is described in [32], but it is beyond the scope of this

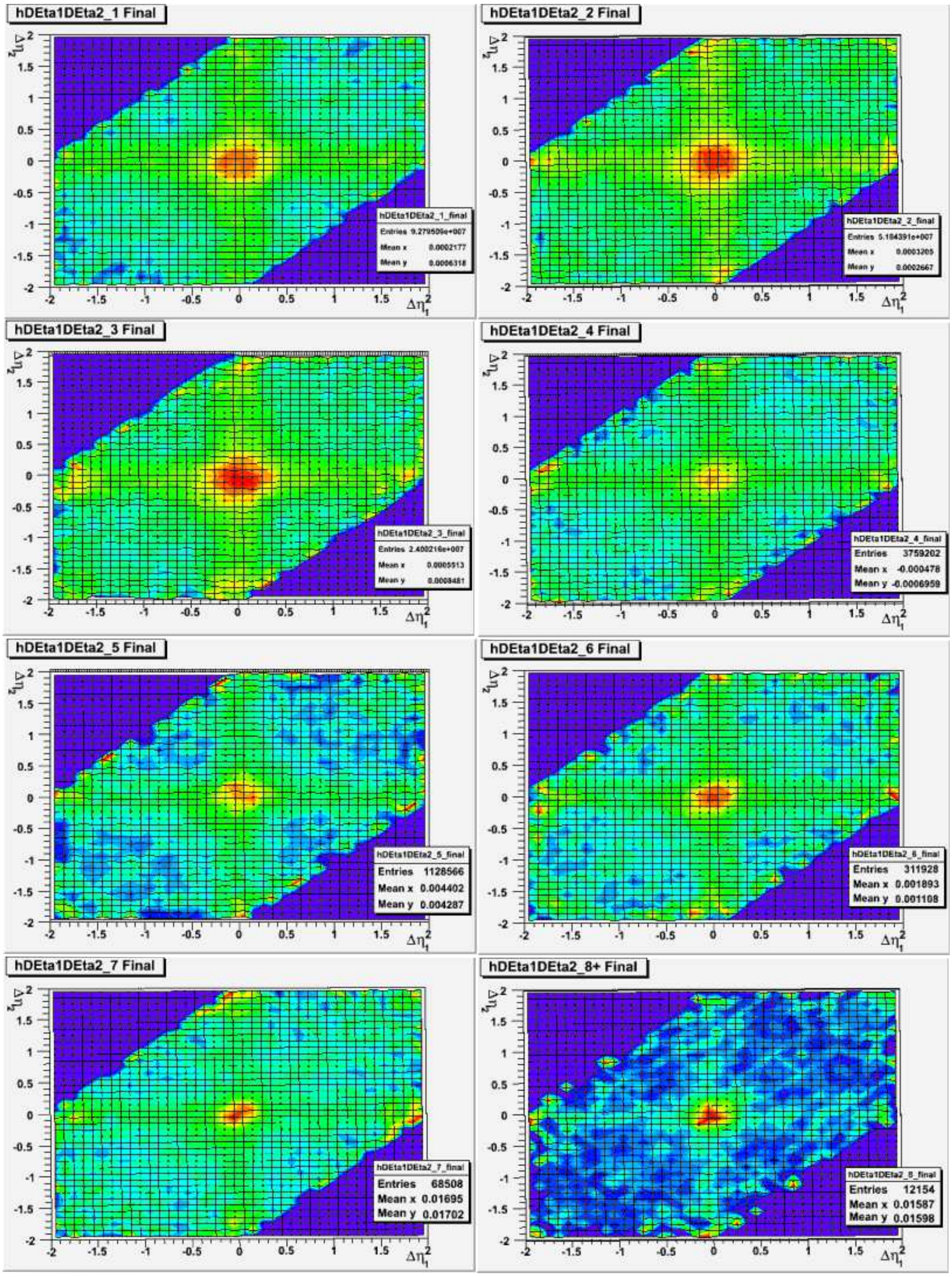

Figure 33: $\Delta\eta_1 \times \Delta\eta_2$ three-particle correlation in all centralities introduced.

thesis to be implemented. Nowadays, this background subtraction is under intense discussion in the STAR collaboration.

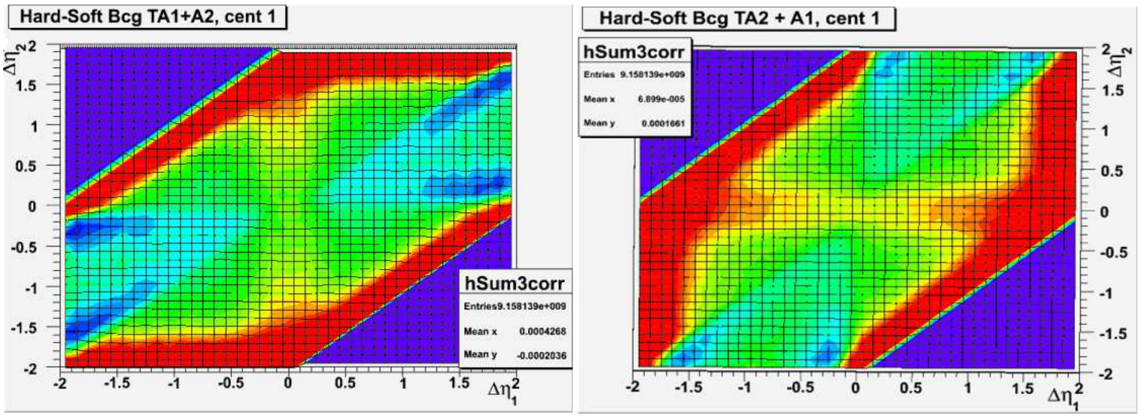

Figure 34: Hard-Soft background contribution created by recording correlate Trigger+Associated1 particle and one random independent Associate2 particle from another event. Left and right picture differs by the selection of random associated particle (A1 or A2).

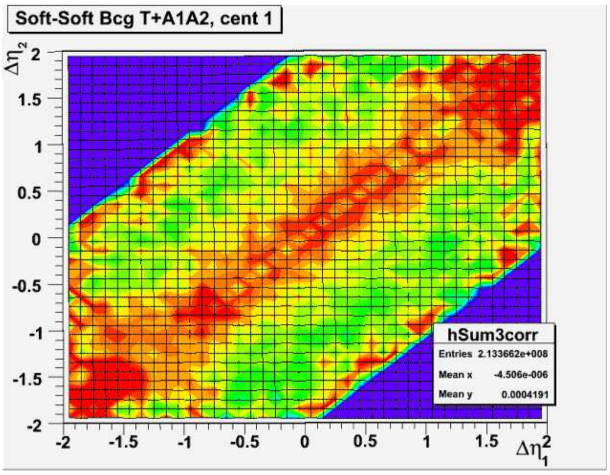

Figure 35: Soft-Soft background contribution created by correlated associated particles A1+A2 with randomly picked trigger from another event.

5 Summary and Conclusion

In this section we will confront the measured three-particle $\Delta\eta_1 \times \Delta\eta_2$ correlations with theoretical models. As already mentioned in the introductory part, several theoretical approaches connect the ridge origin with the presence of the longitudinal flow. The longitudinal flow is supposed to leave a diagonal structure in the $\Delta\eta_1 \approx \Delta\eta_2$ values as schematically drawn in Figure 36-right. The diagonal pattern is created by the preferable collective direction of the associated particles [26]. The drawing contains also a "cross" pattern created by the Hard-Soft background contribution.

If we intend to subtract the background, we have to proceed with extreme caution since the Soft-Soft background has the largest contribution exactly in the diagonal region (Figure 35). Incorrect utilization of Soft-Soft background may lead to canceling the correlation being observed.

The resulting evolution of $\Delta\eta_1 \times \Delta\eta_2$ correlation in all centralities displayed in Figure 33.

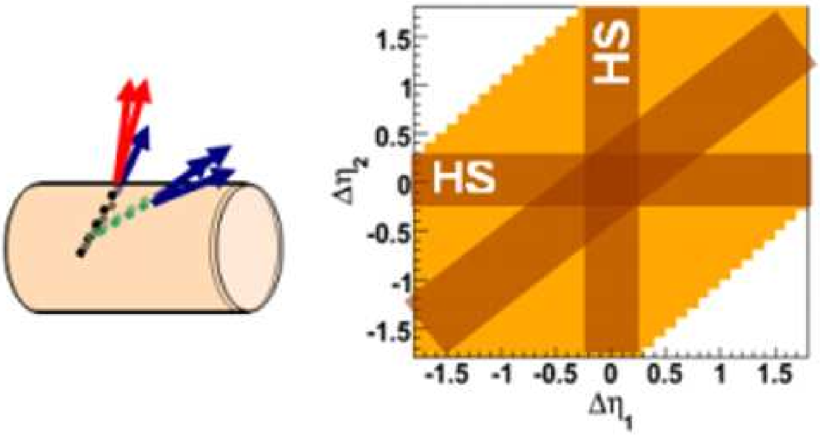

Figure 36: **Left:** Schematics of the deflection of radiated gluons due to the longitudinal flow in hot dense matter. **Right** Sketch of the expected diagonal pattern (due to the preferable collective motion direction) with Hard-Soft contribution.[34]

To measure the on-diagonal anisotropy in comparison to off-diagonal region, Figure 37 shows bin-normalized diagonal yield together with the off-diagonal yield. On-diagonal data are uniform for all $\Delta\eta_1$ data except the near-side jet yield. In comparison with the off-diagonal data, no excess above on-diagonal pattern is observed (Figure 38). The "cross shape" is excluded from the comparison since it is possible to eliminate it by flow-corrected Hard-Soft background subtraction. [32]

In conclusion, our results would not suggest the longitudinal flow presence, because the expected on-diagonal yield is of the same magnitude as the off-diagonal yield. It may be caused by several factors. First, the longitudinal flow is not the correct physics picture for explaining the ridge origin in the hot and dense matter at RHIC. On the other hand, this result would support the other scenarios such as recombination picture [28] or radial flow approach

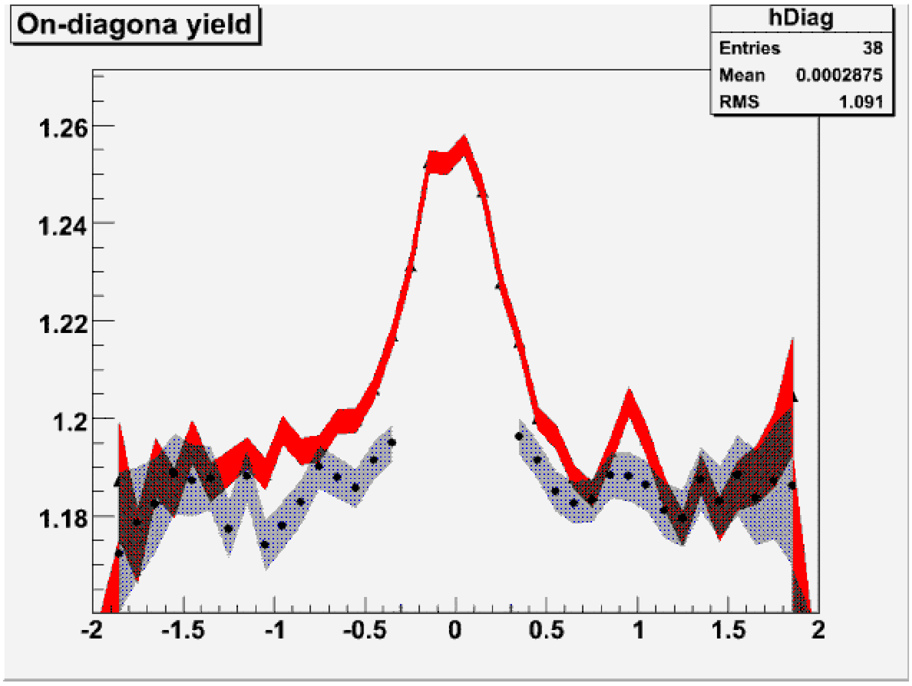

Figure 37: On-diagonal data (blue line) compared to those from off-diagonal (red line) region. The "cross" patern data were left out. The jet contribution is in the middle.

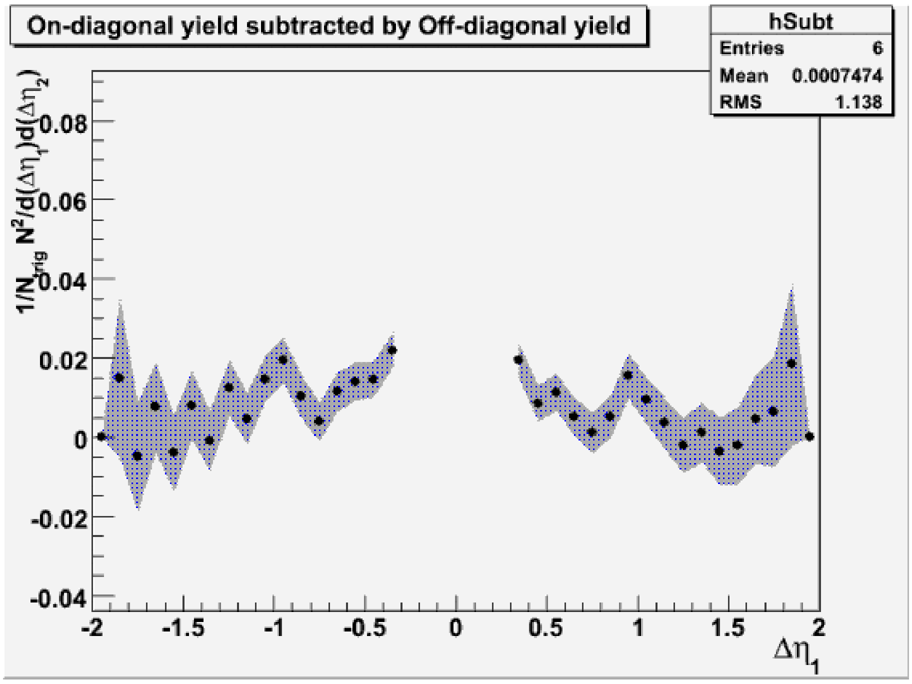

Figure 38: On-diagonal data yield subtracted by the yield from off-diagonal region. The "cross" patern data were left out.

[25],[40]. Second, the data must be studied on more carefully and further investigation is required. Particulary, the subtraction of Hard-Soft and Soft-Soft background contributions including their v_2 and v_4 flow corrections. Furthermore, the high-p_T BEMC triggered data from Run7 may be used to extend the statistics and thus suppress the statistical errors.

Bibliography

[1] "Jörn Putschke" Intra-jet correlations of high-p_T hadrons form STAR, arXiv:nucl-ex/0701074v2, 2007.

[2] "Jana Bielcikova" Two-particle correlations with strange baryons and mesons at RHIC , arXiv:0707.3100v1 [nuccl-ex], 2007.

[3] "Jana Bielcikova" Azimuthal and pseudo-rapidity correlations with strange particles at intermediate p_T at RHIC, arXiv:nucl-ex/0701047v1, 2007.

[4] "K.Yagi et al." Quark-Gluon Plasma, Cambridge Press UK, 2005.

[5] "K.H.Ackermann et al. (STAR Collaboration)" STAR detector overview, Nucl. Instrum. Meth. A 499 (2003) 624-632.

[6] "F. Bergsma et al. (STAR Collaboration)" The STAR detector magnet subsystem, Nucl. Instrum. Meth. A 499 (2003) 633-639.

[7] "R.Bellwied et al. (STAR Collaboration)" The STAR Silicon Vertex Tracker, Nucl. Instrum. Meth. A 499 (2003) 640-651.

[8] "L.Arnold et al. (STAR Collaboration)" The STAR silicon strip detector (SSD), Nucl. Instrum. Meth. A 499 (2003) 652-658.

[9] "M.Anderson et al. (STAR Collaboration)" The STAR time projection chamber, Nucl. Instrum. Meth. A 499 (2003) 650-678.

[10] "M.Anderson et al. (STAR Collaboration)" A readout system for the STAR TPC, Nucl. Instrum. Meth. A 499 (2003) 679-691.

[11] "J.Abele et al. (STAR Collaboration)" The laser system for the STAR time projection chamber, Nucl. Instrum. Meth. A 499 (2003) 692-702.

[12] "L.Kotchenda et al." STAR TPC gas system, Nucl. Instrum. Meth. A 499 (2003) 703-712.

[13] "K.H.Ackermann et al. (STAR Collaboration)" The forward time projection chamber, Nucl. Instrum. Meth. A 499 (2003) 713-719.

[14] "M.Beddo et al. (STAR Collaboration)" The STAR Barrel Electromagnetic Calorimeter, Nucl. Instrum. Meth. A 499 (2003) 725-739.

[15] "J.M.Landgraf et al." An overview of the STAR DAQ system, Nucl. Instrum. Meth. A 499 (2003) 762-765.

[16] "C.E.Allgower et al. (STAR Collaboration)" The STAR endcap electromagnetic calorimeter, Nucl. Instrum. Meth. A 499 (2003) 740-750.

[17] "P.Jones" Making quark matter at Brookhaven's new collider, Europhysics News (2002) Vol.33 No.3.

[18] "S.A. Bass" Probing the QGP at RHIC lesson, Duke University.

[19] "M.Issah, A.Taranenko (PHENIX Collaboration)" Scaling Characteristics of Azimuthal Anisotropy at RHIC, nucl-ex/0604011, 2006.

[20] "PHENIX Collaboration" Scaling properties of azimuthal anisotrophy, PRL 98, 162301(2007).

[21] "STAR Collaboration" Evidence form d+Au measurements for final-state suppresion of hight p_T hadrons in Au+Au collisions at RHIC, nucl-ex/0306024v3, 2003.

[22] "R.J. Porter" Correlations from p-p collisions at $\sqrt{s} = 200GeV$, T.A. Trainor (STAR), arXiv:hep-ph/0506172v1, 2005.

[23] "P. Jacobs (CERN and LBNL group)" Jets in Nuclear Collisions: Status and Perspective, arXiv:nucl-ex/0503022v2, 2005.

[24] "Ch. Wong" Ridge structure in the $\Delta\phi - \Delta\eta$ correlation function associated with a near side jet, Phys. Rew. C76, 054908(2007).

[25] "S.A. Voloshin" Transverse radial expansion in nuclear collisions and two particle correlations, nucl-th/0312065, nucl. phys. A749, 287 (2005).

[26] "N. Armesto et al." Measuring the Collective Flow with Jets, PRL 93, 242301, 2004.

[27] "A.Majumber, B. Müller, S.A. Bass" Longitudinal Broadening of Quenched Jets in Turbulent Color Fields, hep-ph/0611135v2, 2007.

[28] "Ch.B. Chiu, R.C. Hwa" Pedastal and Peak Structure in Jet Correlation, nucl-th/0505014v1, 2005.

[29] "J.Adams et at. STAR Collaboration" Measurements of transverse energy distribution in Au+Au collisions at $\sqrt{s_{NN}} = 200GeV$, Phys. Rev. C 70, 054907, 2004.

[30] "J.Adams et a. STAR Collaboration" Evidence from d+Au Measurements for Final-State Suppresion of High-p_T Hadrons in Au+Au Collisions at RHIC, Phys. Rev. Lett. Volume 91, Issue 7, 2003.

[31] "NN.Ajitanand et al." Decomposition of Harmoinc and Jet Contributions to Particle-pair Correlations at Ultra-relativistic Energies, Phys. Rev. C72, 011902, 2005.

[32] "J.G. Ulery, F.Wang" Analysis Method for Jet-Like Three-Particle Azimuthal Correlations, nucl-ex/0609016v2, 2008.

[33] "Hydrodinamic Flow from Fast Particles" J. Casalderrey-Solana, E. V. Shuryak, D. Teaney, hep-ph/0602183, 2006.

[34] "Pawan Kumar Netrakanti" Quark Matter 2008 talk, *http : //www.star.bnl.gov/protected/spectra/pawan/Correlation/web/Paper/index.htm.*

[35] "Roy J. Glauber" Lectures in Theoretical Physics, Interscience, N.Y., 1959.

[36] "S. Voloshin, Y. Zhang" Z.Phys C70, 665, 1996.

[37] "M. Guylassy et al." Jet Quenching and Radiative Energy Loss in Dense Nuclear Matter, nucl-th/0302077, 2003.

[38] "Mark J. Horner" Systematic Studies of Low- and Intermediate-p_T Correlated Angular Distributions in Au+Au Collisions at $\sqrt{s_{NN}} = 200$ GeV from the STAR Experiment, Ph.D. thesis, University of Cape Town, 2007.

[39] "Jason Glyndwr Ulery" Two- and Three-Particle Jet-Like Correlations, Ph.D. thesis, Purdue University, 2007.

[40] "E. Shuryak" On the Origin of the "Ridge" phenomenon induced by Jets in Heavy Ion Collisions, 0706.3531 [nucl-th], 2007.

[41] "Star trigger web page"
$http : //www.star.bnl.gov/protected/common/common2004/trigger2004/triggers2004.html$

[42] "R. Brun et al." ROOT, an Object Oriented Data Analysis Framework, http://root.cern.ch/.

[43] "J. Putschke (for STAR Collaboration)" Quark Matter Talk 2006, Shanghai, 2006. 32, L37.

[44] "L. Gaillard" A Study of Jets at the STAR Experiment at the Relativistic Heavy Ion Collider via Two-Particle Correlations, Ph.D. thesis at University of Birmingham, 2008.

[45] "P. F. Kolb" Early Thermalization and Hydrodynamic Expansion in Nuclear Collisions at RHIC, Ph.D. thesis, Universität Regensburg, 2002.

Acknowledgements

I am very thankful to my supervisor Jana Bielčíková for her invaluable help, guidance and patient listening to my countless questions. I would like to thank also Jaro Bielčík for his hints when the work was not progressing well. Special thanks goes to the group of the Experimental Nuclear Physics at our faculty for keeping warm and friendly atmosphere as well as the creative environment.